Ares: A Coupling Methodology for Ablation Modeling

Olivia M. Schroeder*, Joseph C. Schulz†, Georgios Bellas-Chatzigeorgis‡, Prakash Shrestha§, Grant Palmer¶
Analytical Mechanics Associates, Inc., Moffett Field, CA, 94035

Joseph M. Brock, ‖
GoHypersonic Inc., Minneapolis, MN, 55413

Eric C. Stern **
NASA Ames Research Center, Moffett Field, CA, 94035

Graham V. Candler ††
University of Minnesota, Minneapolis, MN, 55455

To enable modeling of complex and coupled ablation problems, a multi-physics framework is developed. A methodology for modeling shape change in coupled systems is presented. The approach taken to model gas-surface interactions and translate coupled surface phenomena to physically meaningful boundary conditions in the distinct solvers is discussed. Particular emphasis is placed on the nature of coupled boundary conditions pertaining to surface energy and mass balances as well as surface chemistry modeling. The developed methodology is used to simulate a shear test in arc-jet conditions in order to assess the validity of the coupled approach as well as the implementation of the relevant physical processes.

I. Introduction

Ablating thermal protection systems (TPS) are required in order to maintain the integrity of spacecraft during high-speed entry. As the kinetic energy of the spacecraft is dissipated in the form of radiative and convective heat transfer to the surface, ablative materials provide mechanisms for attenuating a portion of that energy. These mechanisms include pyrolysis and the subsequent convective transfer of energy within the fibrous matrix by pyrolysis gas products, displacement of the boundary layer due to blowing, and thermochemical ablation of carbon (oxidation, nitridation, and sublimation). In order to correctly characterize the performance of these TPS systems, both computational fluid dynamics (CFD) and material response simulations are required. Modeling assumptions based on the differences in the material and flow time scales may justify a decoupled approach whereby CFD simulations are used to extract an approximate boundary condition for a separate material response simulation. Since the material response is dependent on integrated heat load, time-dependent boundary conditions must be extracted from a series of steady-state CFD solutions. The process is approximate and does introduce error, particularly when significant shape change occurs. In a coupled approach, information at the interface between the material and the fluid is exchanged directly and synchronized at whatever frequency the physics requires to achieve time-accuracy. This work describes the development of Ares that specifically couples the US3D flow and Icarus material response solvers, but within the larger context of modeling entry systems, the methodology employed within Ares only depends on a material and flow physics kernel. Ares manages the exchange of data in a physically meaningful manner while maintaining computational feasibility of multi-physics calculations.

*Research Scientist, AIAA Member
†Research Scientist, AIAA Member
‡Research Scientist, AIAA Member
§Research Scientist, AIAA Member
¶Research Scientist, AIAA Associate Fellow
‖Research Scientist, AIAA Member
**Research Scientist, AIAA Senior Member
††Professor, AIAA Fellow

II. Algorithm

US3D is an unstructured, finite-volume, compressible Navier-Stokes solver [1–3] and employs a plug-in architecture to provide a mechanism for modifying the physics of the governing equations via adjustments to boundary conditions, source terms, and fluxes. Ares is such a plug-in and couples Icarus [4], an unstructured, finite-volume solver for material response, to the evolution of the flow. Ares performs the data exchange between US3D and Icarus and controls the ordering of operations for all participating physics kernels. This provides a desirable balance between flexibility of time-scale management (tightness of coupling) while also allowing for a low-level control of how data participate and are exchanged at the fluid-material interface.

Ares currently consists of a collection of objects that hold the methods necessary for solving their respective system. Figure 1 depicts the general objects that Ares operates on, the flow of operations and dependencies, and some of the methods contained within each object. The time manager contains objects to store data and methods associated with the

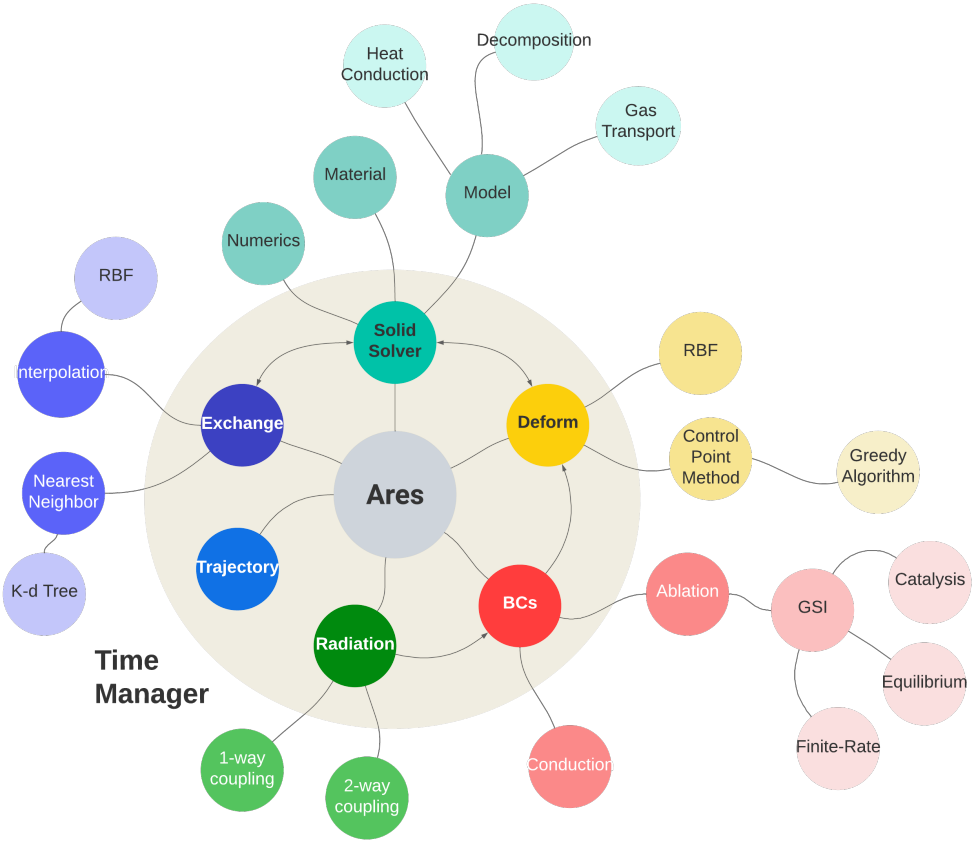

Fig. 1 Ares Components.

scheduling of the different physics kernels. For example, the trajectory or inflow conditions and the material response solver are defined as functions of time, while the flow and radiation solvers are often managed via an iteration-based convergence scheduling. The time manager takes user-defined inputs to control each physics solver, relates all of these quantities to the physical time of the simulation, and enforces a prescribed tolerance level for converging the coupled physics. Details of how time-management is done in the context of disparate time-scales is covered in Section III.

The data manager contains the parallel communication infrastructure used to exchange and reconstruct n-dimensional, large sparse data sets between all solvers. There are three main physics solvers managed by Ares: fluid dynamics (US3D), material response (Icarus), and radiation (NERO) [5, 6]. While Ares interacts with Icarus and NERO through objects, interfacing with US3D is done through handlers at discrete positions during the flow solve because of the plugin structure. A complex set of physical mechanisms drive the interaction between the flow and the ablating material. Accounting for shape change as well as the thermo-chemical processes involved within the mass and energy balances requires careful consideration within the boundary conditions of US3D and Icarus. Details of the various coupled

boundary conditions are explained in Section V. Shape change can occur if a heat shield is ablating and this can significantly affect the heating distribution on the surface. To capture this, mesh motion is employed via the algorithm described in Section VI.
Figure 2 shows how the physics kernels relate to each other and the flow of information between them.

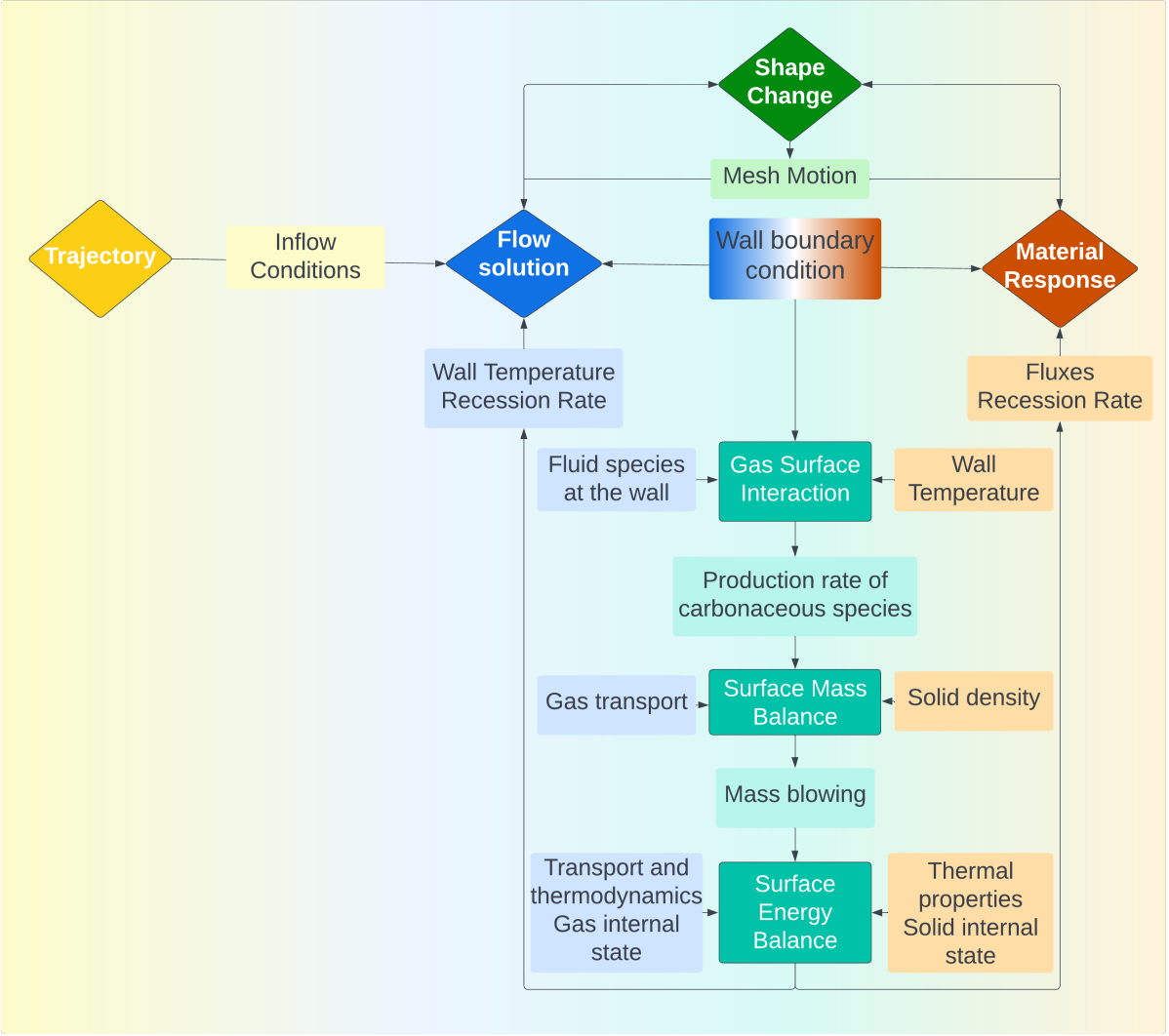

Fig. 2 Diagram of physics interactions.

III. Time-Scale Management

A complete simulation of all the physics involves a range of time scales. One of the most important time scales is the one associated with the trajectory of the vehicle. This determines the total time required to simulate the material response. The next consideration is the time scale associated with the thermochemical processes occurring at the surface between the material and the boundary layer flow. This includes the ablation rate, the balance of convection and diffusion of species to and from the surface, and the kinetics of the surface reactions. The time scales associated with these processes determine the frequency at which the surface energy and mass balances need to be updated to ensure accurate boundary conditions for the material response. Other physical processes related to the residence time of flow along the surface of the vehicle within the boundary layer are also important, but more difficult to quantify. Because of the complexity of the physical interactions, it is expected that relative importance of the time scales is application

dependent, e.g., simulations of arcjet material response will likely have different time scale considerations for coupling than Earth or Mars entry vehicle simulations. Additionally, assumptions can be made to relax constraints to make coupled simulations amenable for engineering applications. User control over the time management of the different physics kernels is therefore important.

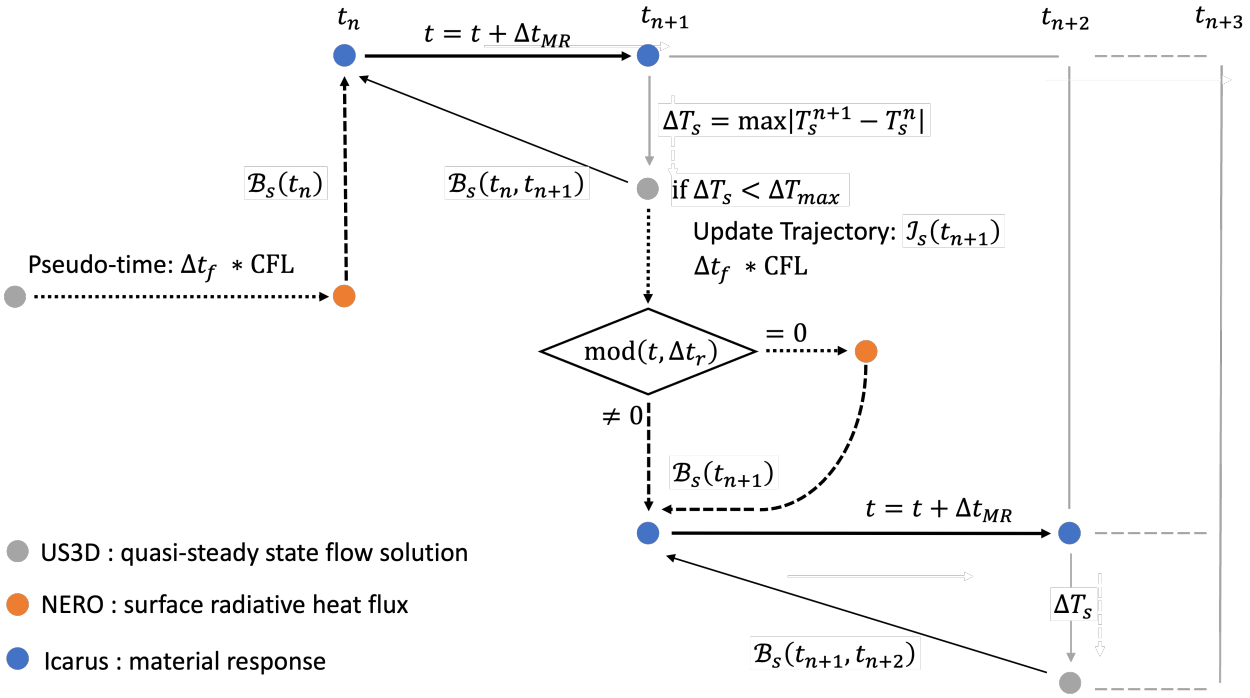

Fig. 3 Participating time scales.

Ares currently allows users to specify a schedule for when the material response, the radiative field, and the flow field are updated. Figure 3 is an illustration of the process, which can be depicted as a series of three events. First, US3D converges the flow to a quasi-steady state at time t_n. Second, NERO computes the radiative heat flux at the surface. One-way coupling is assumed in the diagram for simplicity, but it is possible to converge the flow and radiative fields to a quasi-steady state using a series of US3D-NERO iterations. The third step then involves passing the time-dependent boundary state, $B_s(t_n)$, to Icarus. The physical time of the coupled simulation is advanced by the material response and a new boundary state is computed, $B_s(t_{n+1})$. The updated boundary state is different than that used to converge the flow, and the boundary conditions used by US3D and Icarus can be physically inconsistent. Whether the inconsistency results in significant errors in the prediction of the in-depth material response is a function of the relative importance of the time scales discussed in the previous paragraph. The error can be related to difference between the surface temperatures at the two time instances. In reference to Fig. 3, if ΔT_{max} is very large, then coupling can be referred to as explicit, i.e., only a single pass of the material response simulation is completed since the temperature difference at the surface is always less than the prescribed convergence criteria. Otherwise, an "implicit" coupling strategy is employed [7]. In this scenario, the flow is re-converged to a quasi-steady state using the $B_s(t_{n+1})$ state as predicted by the material response, and then Icarus is restarted from time t_n with the material response boundary conditions applied such that the boundary state is linearly interpolated from $B_s(t_n)$ to $B_s(t_{n+1})$. This process is continued until the convergence criteria is met. Only then is the time advancement, $t_{n+1} = t_n + t_{MR}$, accepted where t_{MR} is the material response time and can change during the simulation. After a completion of the first cycle, the inflow conditions are updated based on the current physical time, and NERO updates the radiative field based on a prescribed time frequency, Δt_R. This process continues until the total physical time is reached. Note that the flow convergence to quasi-steady state is set using a user-defined number of iterations.

IV. Data Exchange

Since the governing equations of the flow, the material, and the radiative field are solved on separate computational domains or grids, coupling requires transferring information between these domains. Various approaches have been adopted to accomplish this. The simplest method is to use information about how the computational domains are constructed to generate a one-to-one mapping between the elements of each domain, i.e., face-matching grids. The approach has trivial computational cost (ignoring parallel communication costs) and zero error at the exchange. However, the requirement of one-to-one mapping is undesirable for complex geometries since the distinct physics solvers can have very specific meshing requirements (for gradient reconstruction, mesh motion, boundary layer cell spacing and aspect ratio, to name a few examples). Additionally, while a generalized method to build a one-to-one mapping between the domains is possible, more naive approaches often rely on specific details of the mesh construction and are less general.

An improvement to this methodology is to use nearest-neighbor searches where the data within each domain is represented as a point-could distribution. Only the coordinates of the source and target points are required, which relaxes the face-matching requirement. Brute-force, nearest-neighbor searches can become costly on large grids; however, there are many algorithms which can be employed to speed-up the searches such as kd-trees, oct-trees, or ball-trees. Finally, it should be noted that while face-matching is not a requirement, the error as it relates to the projection of a variable from one neighbor to the next increases as the distance and spatial variation between them increases. This point will be illustrated in the following section. A common method to reduce error from misaligned source and target data is to perform interpolation. There are many interpolation methods, and the accuracy, complexity, and cost of each method depends of on the problem and the implementation. In this work we will focus on one method: radial basis function interpolation.

Finally, it is worth mentioning that the area of overlap approach commonly used for conjugate heat transfer [8, 9] offers a very accurate, fully-conservative approach to exchanging data for flow and material response coupling. In this approach, the surface grid on one domain is projected onto the other, and the area of overlap between the faces of the two domains is computed using a Sutherland-Hodgeman algorithm [10]. For example, consider the variable ϕ of domain a projected to domain b. It can be represented by the sum of the fractional areas of overlap of all faces with non-zero contribution

$$\phi_j = \sum_{i=1}^{N_f} \frac{A_{o_{a,b},i}}{A_{b,j}} \tag{1}$$

where N_f is the number of faces of domain a with non-zero overlap with a face of domain b, and $A_{o,i}$ is the area of overlap of face i of domain a with face j of domain b. The method is more complex to implement, particularly for time-evolving, partitioned data where the area of overlap requires a changing list of faces as the topology of the interface changes. Implementing this algorithm, however, is a future work goal for the Ares framework.

A. Radial Basis Function Interpolation

The radial basis function (RBF) interpolation [11] is of the form

$$s(\mathbf{r}) = \sum_{i=1}^{N} \alpha_i \phi(||\mathbf{r} - \mathbf{r_i}||) \tag{2}$$

where $s(\mathbf{r})$ is the interpolated variable at a point at location $\mathbf{r}$ in space, $\phi(||\mathbf{r} - \mathbf{r_i}||)$ is the basis function evaluated at the distance between a source point $\mathbf{r_i}$ and the target point $\mathbf{r}$, and α_i are the weight coefficients associated with each source point. The implementation of the method presented herein follows that of Rendall and Allen [12].

The weight coefficients α_i in Eq. 2 are unknown and must be determined. The entire solution process can be recast as a two-step method. First, a linear system is constructed,

$$s(\mathbf{r})_s = \mathbf{M}\boldsymbol{\alpha} \tag{3}$$

where

$$\mathbf{M} = \begin{pmatrix} \phi_{s_1 s_1} & \phi_{s_1 s_2} & \cdots & \phi_{s_1 s_{N_t}} \\ \phi_{s_2 s_1} & \phi_{s_2 s_2} & \cdots & \phi_{s_2 s_{N_t}} \\ \vdots & \vdots & \ddots & \vdots \\ \phi_{s_{N_t} s_1} & \phi_{s_{N_t} s_2} & \cdots & \phi_{s_{N_t} s_{N_t}} \end{pmatrix} \tag{4}$$

and ϕ is the adopted radial basis function whose argument is the Euclidean norm

$$d = \sqrt{(x - x_i)^2 + (y - y_i)^2 + (z - z_i)^2}. \tag{5}$$

By solving this system, $\boldsymbol{\alpha}$ is determined. The second step involves a matrix-vector multiplication operation that computes the interpolated variable on the target points using the weight coefficients previously determined,

$$s(\mathbf{r})_t = \mathbf{A}\alpha \tag{6}$$

where

$$\mathbf{A} = \begin{pmatrix} \phi_{s_1 t_1} & \phi_{s_1 t_2} & \cdots & \phi_{s_1 t_{N_t}} \\ \phi_{s_2 t_1} & \phi_{s_2 t_2} & \cdots & \phi_{s_2 t_{N_t}} \\ \vdots & \vdots & \ddots & \vdots \\ \phi_{s_{N_s} t_1} & \phi_{s_{N_s} t_2} & \cdots & \phi_{s_{N_s} t_{N_t}} \end{pmatrix} \tag{7}$$

To reduce computational cost, the calculation of the weight coefficients $\boldsymbol{\alpha}$, which is the most expensive portion of the solve, is done only once at initialization and these are re-used for each exchange of data. In this way, the full cost of the method amounts to two linear system solves, one for each set of sources and targets (fluid to solid and solid to fluid), and $2N_{\text{exchanges}}$ times matrix-vector product. In the current implementation, the PETSc linear algebra package [13] is used for solving the linear systems in parallel using ILU-0 factorization and Generalized Minimal Residual Method (GMRES). The selection of basis function is an important consideration as it significantly affects accuracy and cost. As will be described in a later section, the same methodology used for the surface data interpolation is used for the mesh motion scheme; however, the types of basis functions employed are different. There are three types of basis functions: global, local, or compact. Briefly, global functions are always non-zero and grow with distance to the source point. Local functions are largest at the source point and decay with distance but are always non-zero at finite-distance. Compact functions share the decay over distance property of local functions and are zero at a finite-distance, a distance referred to as the base radius or compact support R. Compact support reduces the computational cost of the linear solve by introducing sparsity to the system since several off-diagonal terms in the $\mathbf{M}$ and $\mathbf{A}$ matrices become zero. For this application it is desirable to have the local character both for the decaying property (closest source points have the largest weight) and sparsity; thus, compact functions are preferred. For data exchange in Ares, the following basis function is used

$$\phi = 1 - \frac{||\mathbf{r}||}{R}. \tag{8}$$

B. Data Reconstruction

In order to assess the error properties of the RBF method for the current application an arbitrary variable is defined, ψ, with a known analytical form, in this case

$$\psi = \sin\left(\pi\theta + \frac{\pi}{2}\right) \tag{9}$$

where θ corresponds to the angle of a given point on the surface of a cylinder. Computational meshes are constructed for the fluid and solid domains with the fluid grid containing $N_f = 180$ surface points. A set of solid grids are constructed at four sizes, specifically $N_s = \{30, 60, 180, 360\}$ surface points. The goal is to assess the accuracy of the reconstruction of Eq. 9 on the target mesh for different degrees of mismatch in the grids. Figure 4 shows the interpolation using RBF, where Fig. 4a corresponds to a fine-to-coarse interpolation, Fig. 4b shows the interpolation between face-matched grids, and Figs. 4c and 4d correspond to coarse-to-fine interpolations. Figure 4 suggests that the RBF interpolation reconstructs the data extremely well even from very coarse grids except near the edges. This is known as Runge's phenomenon in interpolation [14]. Figure 5 shows the reconstruction using nearest-neighbor, i.e., no interpolation is used. It is clear from Figs 5c and 5d that as the distance between source points increase, the reconstruction deteriorates resulting in a stair-stepped profile. Figure 6 shows the error in both methodologies for the coarsest grid level. While the RBF method requires a solution for the edges, it offers a significant improvement over the nearest-neighbor approach. The nearest neighbor method presents low error at points where targets are close to the source but rapidly increases as the distance to the target increases. This is most apparent near the high angular positions on the cylinder where the distance between points increases (grid coarsens).

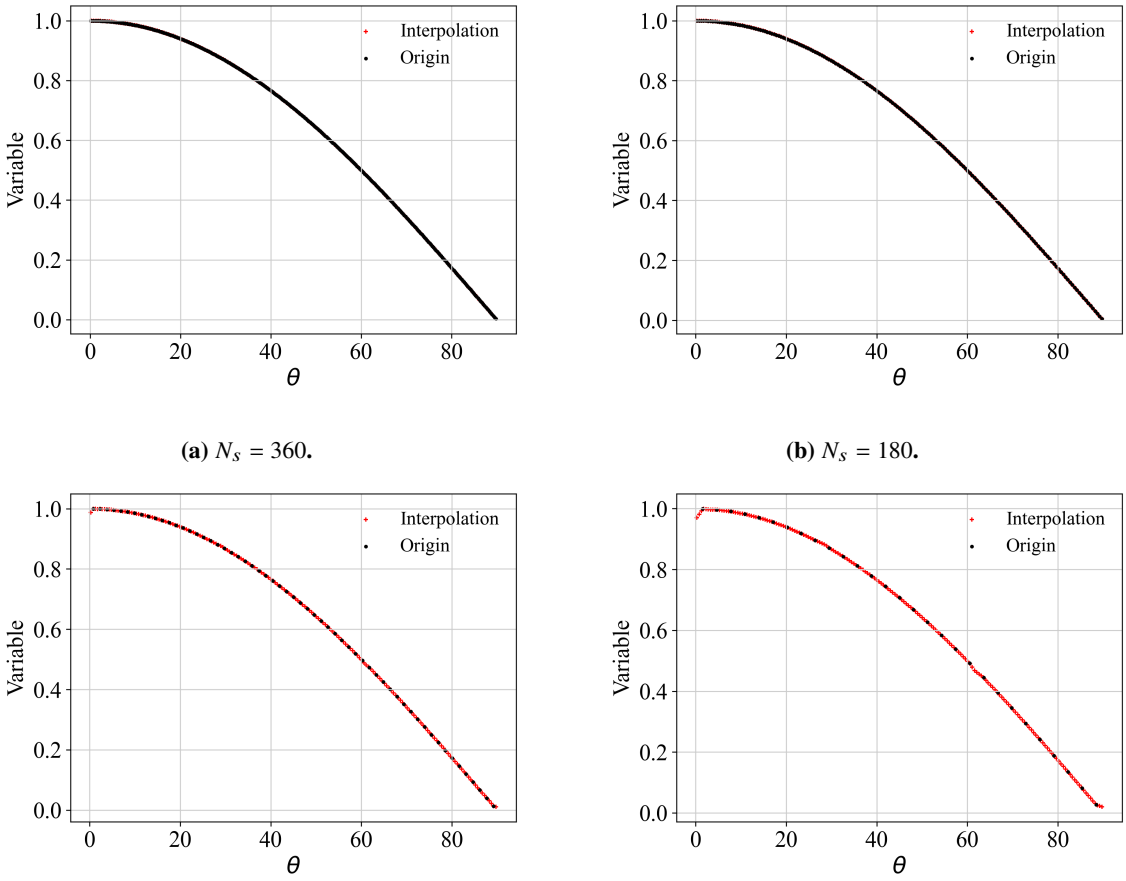

(a) $N_s = 360$. **(b)** $N_s = 180$.

(c) $N_s = 60$. **(d)** $N_s = 30$.

Fig. 4 RBF interpolation.

V. Coupled Boundary Conditions

A. Primer on coupled boundary conditions

The methodology presented solves the governing equations of the flow and the material separately within distinct fluid and solid domains, which means that the respective boundary conditions within each domain are evolved at distinct time scales. This is contrary to a unified approach [15–17], where a single set of governing equations is solved for both gas and solid phases with the interface between the phases treated as a sharp discontinuity. The benefit of the approach is that the total mass and energy is consistently conserved, but it can be computationally expensive. By treating the fluid and solid domains distinct and separating the governing equations in each, the computational framework is simplified, but the pursuit of a consistent boundary condition between the domains is more challenging. By a consistent boundary condition we mean a boundary condition that evolves at the time scale of time-advancement (in this case the time step of the material response). This requires that the adjacent domains be updated at the given time level. The implication of this is that either the flow domain must be time-accurate and the material response is advanced at significantly smaller time increments than allowed by the time scheme, or the flow field is converged to quasi-steady state at the material response time-step [18]. Some methodologies leverage pseudo-time stepping of the material response to gain computational efficiency [19, 20], and the implicit formulation of the coupled boundary conditions can enlarge the allowable time-step size of the material response at a given fluid state [21]. These methods have been shown to reduce oscillations of the surface quantities observed between coupling updates for high heat fluxes or recession rate problems [22], or varying inflow conditions. However, they can sometimes be cost prohibitive for problems of long exposure time and are not always necessary in the steady-state ablation regime.

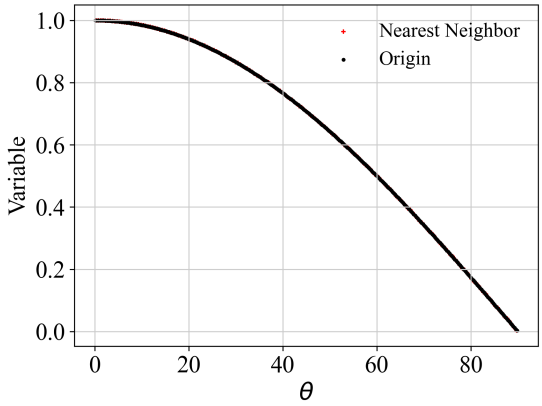

(a) $N_s = 360$**.**

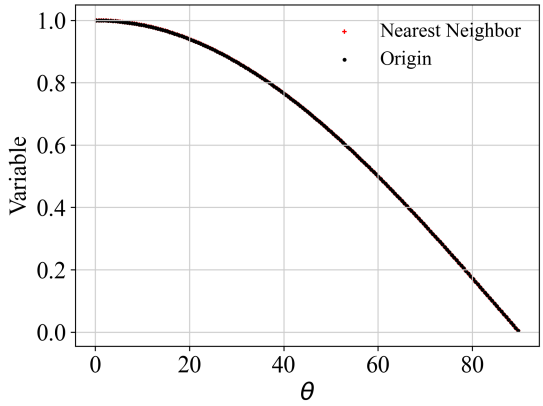

(b) $N_s = 180$**.**

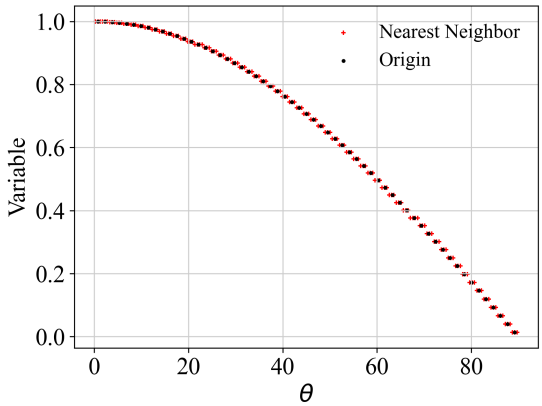

(c) $N_s = 60$**.**

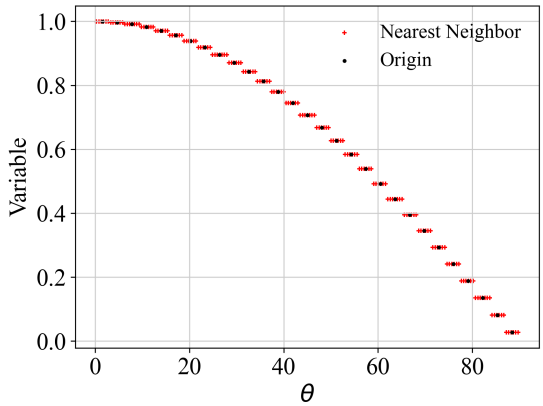

(d) $N_s = 30$**.**

Fig. 5 Nearest neighbor interpolation.

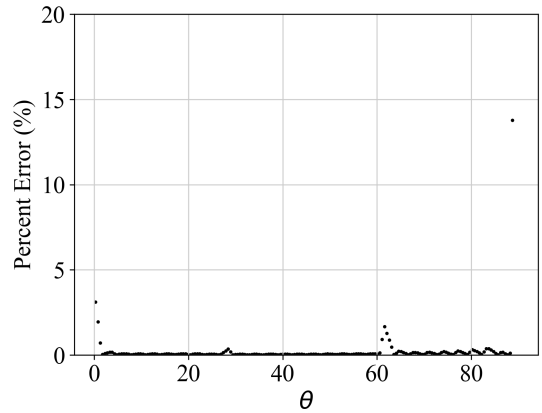

(a) RBF interpolation.

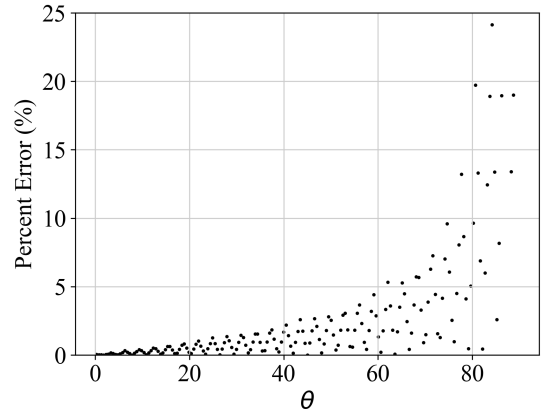

(b) Nearest neighbor.

Fig. 6 Error in interpolation with $N_s = 30$**.**

B. Surface Balances

At the surface, conservation laws require that the mass and energy fluxes across the interface be balanced. These balance equations have been described previously in the context of aerothermodynamics [23–26]; however, the details of how the boundary conditions should be implemented are varied due to the diversity of approaches in numerical schemes and time-advancement of coupling or the coupled sub-systems. Conservation of energy at the gas-solid interface requires that in the frame of reference of the surface the fluxes from the fluid are balanced with the fluxes from the solid,

$$\underbrace{F_f}_{\text{Fluid Energy Fluxes}} - \underbrace{F_c}_{\text{Material Energy Fluxes}} = 0, \tag{10}$$

where subscripts f and c are for fluid and solid phases, respectively. Using the Navier-Stokes equations, the fluid flux is determined as

$$F_f = \underbrace{\sum_{n=1}^{N_m}(-\kappa\nabla T)_n}_{\text{Conduction}} + \underbrace{\sum_{i=1}^{N_s}(J_i h_i)}_{\text{Diffusion}} + \underbrace{\rho u h}_{\text{Advection}} + \underbrace{\tau:\mathbf{u}}_{\text{Viscous Stress}} + \underbrace{q_{\text{rad,in}}}_{\text{Radiation}}, \tag{11}$$

where subscript n corresponds to the energy mode in N_m modes, and N_s is the number of gaseous species. The energy equation in the ablating surface frame of reference determines the solid flux,

$$F_c = \underbrace{-\kappa_c\nabla T}_{\text{Conduction}} - \underbrace{\phi\rho_{pg}h_{pg}u_{pg}}_{\text{Pyrolysis Flow}} - \underbrace{\rho_c h_c u_c}_{\text{Moving Surface}} + \underbrace{(1-\alpha)\dot{q}_{\text{rad}}}_{\text{Absorbed Radiation}} - \underbrace{\sigma\epsilon T_w^4}_{\text{Re-Radiation}}, \tag{12}$$

where subscript pg stands for pyrolysis gas and w for wall. It is common for fluid simulations relevant to this work to employ Park's two-temperature model where translation-rotational and vibrational-electronic energy modes of the gas are assumed to be in thermal equilibrium with each other, described by T_{tr} and T_{ve}, respectively [27]. However, it is generally assumed that the wall is in thermal equilibrium $T_w = T_{tr} = T_{ve}$. For laminar flows, viscous stresses are typically small relative to other terms and are currently neglected. Thus, applying these simplifications to Eq. 11 and revisiting Eq. 10, the generic energy balance becomes

$$\begin{aligned} -\kappa_{tr}\nabla T_{tr} - \kappa_{ve}\nabla T_{ve} + \sum_{i=1}^{N_s}(J_i h_i) + \rho u h + q_{\text{rad,in}} = \\ -\kappa_c\nabla T + \phi\rho_{pg}h_{pg}u_{pg} + \rho_c h_c u_c + \alpha\dot{q}_{\text{rad}} - \sigma\epsilon T_w^4. \end{aligned} \tag{13}$$

A similar argument can be made for the species mass balances. The net flux for each gaseous species from the gas and pores of the solid phases is equal to their chemical rate due to heterogeneous reactions,

$$\underbrace{W_{f,i}}_{\text{Fluid Mass Fluxes}} - \underbrace{W_{c,i}}_{\text{Material Mass Fluxes}} = \underbrace{w_i}_{\text{Chemical Reactions}}. \tag{14}$$

The fluid mass fluxes are retrieved from the species continuity equation,

$$W_{f,i} = J_i + \rho_i u, \tag{15}$$

and the mass fluxes of the pyrolysis gas species from the solid phase is

$$W_{c,s} = \phi\rho_{pg,i}u_{pg}. \tag{16}$$

The chemical source term is equal to the sum of heterogeneous catalytic and ablative reactions, expressed as

$$w_i = \sum_{k=1}^{N_r}\dot{\omega}_{k,i}M_i, \tag{17}$$

where N_r, is the total number of reactions that species i participates in. By replacing the closures in Eq. 14 one gets

$$J_i + \rho_i u - \phi \rho_{pg,i} u_{pg} = w_i. \tag{18}$$

When summing only over the gaseous species, the mass balance becomes

$$\sum_{i=1}^{Ns} (\rho_i u - \phi \rho_{pg,i} u_{pg}) = \sum_{i=1}^{Ns} w_i. \tag{19}$$

The sum of the diffusive fluxes must be zero, $\sum_{i=1}^{Ns} J_i = 0$, to prevent diffusion velocities from becoming ill-posed [28, 29]. Returning to Eq. 19, this results in

$$\rho u - \phi \rho_{pg} u_{pg} = \sum_{i=1}^{Ns} w_i. \tag{20}$$

It will be useful in later sections to multiply Eq. 19 by the species enthalpies calculated at the wall temperature, resulting in

$$\sum_{i=1}^{Ns} (J_i h_i + \rho_i u h_i - \phi \rho_{pg,i} u_{pg} h_i) = \sum_{i=1}^{Ns} w_i h_i. \tag{21}$$

The generic forms of the surface balances have now been presented for an interface connecting the flow of a chemically reacting, multi-temperature gas, with a porous, ablating and pyrolyzing solid. From here simplifications can then be applied to retrieve the different types of interfaces available in Ares, which are useful for a variety of aerospace applications.

1. Inert and Impermeable Surface

Consider a chemically inert, impermeable surface. In the absence of chemical reactions all species have $w_i = 0$, and the impermeability constraint imposes $\phi \rho_{pg} u_{pg} = 0$. As a result, we retrieve $\rho u = 0$, and Eq. 21 simplifies to

$$\sum_{i=1}^{Ns} J_i h_i = 0, \tag{22}$$

with the total energy reducing to a heat flux-radiation balance as

$$-\kappa_{tr} \nabla T_{tr} - \kappa_{ve} \nabla T_{ve} + q_{\text{rad,in}} = -\kappa_c \nabla T + \alpha \dot{q}_{\text{rad}} - \sigma \epsilon T_w^4. \tag{23}$$

2. Catalytic and Impermeable Surface

The dissociated species produced by the high-enthalpy flows tend to recombine in the boundary layer and at the material surface where the surface acts as a third-body catalyst. This is usually an exothermic process and contributes to the heating of the surface and increases the diffusive part of the total heat flux. The rate of mass production or destruction of species i at the surface in the absence of any ablative reactions is given by

$$w_i = \sum_{k=1}^{N_r} \dot{\omega}_{k,i,\text{cat}} M_i = \sum_{k=1}^{N_r} \nu_{k,i} r_k M_i, \tag{24}$$

where ν_{ki} and r_k are the stoichiometric coefficients and rates of progress for each reaction (subscript r), summed over all catalytic reactions N_r for each species i. Catalytic reactions, contrary to ablation, conserve total mass giving

$$\sum_{i=1}^{Ns} w_i = 0. \tag{25}$$

With the impermeability condition, $\rho u = 0$. As a result, the energy balance in Eq. 34 can be simplified to

$$-\kappa_{tr} \nabla T_{tr} - \kappa_{ve} \nabla T_{ve} + \sum_{i=1}^{N_s} (J_i h_i) + q_{\text{rad,in}} = -\kappa_c \nabla T + \alpha \dot{q}_{\text{rad}} - \sigma \epsilon T_w^4. \tag{26}$$

The equation above needs to be solved in conjunction with the species surface mass balance, $J_i = \omega_i$, to retrieve the gas composition at the surface at a consistent surface temperature. Details on this process will be given later in this work when numerical methods for the solution of the surface balances is discussed.

3. Non-Pyrolyzing Ablating Surface

In addition to catalytic recombination reactions, carbon-based TPS materials undergo surface ablation reactions. In this case, gaseous species containing oxygen and nitrogen atoms react with the solid carbon at the surface and produce carbon bearing molecules, such as CO, CO_2, and CN. At higher temperatures, the carbon matrix can also sublimate, producing carbonaceous species like C, C_2, C_3, C_5. Starting with the total mass balance Eq. 20 and invoking the same assumptions as in the catalytic surface, one can retrieve that the result that the total mass injected into the gas is equal to the mass loss during ablation,

$$\rho u = \sum_{i=1}^{N_s} w_i = \dot{m}_c. \tag{27}$$

Contrary to the purely catalytic case, the sum over all gaseous species is non-zero since mass is added from the solid surface to the flow. Relating the mass loss rate to the material density, one can obtain the wall velocity (or recession rate) as

$$\dot{s} = \frac{\dot{m}_c}{\rho_c} = \frac{\sum_{i=1}^{N_s} w_i}{\rho_c}. \tag{28}$$

The blowing velocity is given by the conservation of mass constraint as

$$u_w = \frac{\dot{m}_c}{\rho_w}, \tag{29}$$

where the subscript w corresponds to a gas-phase quantity at the wall. The large discrepancy between the solid and gaseous densities accelerates the recession rate of a few micrometers a second to a blowing velocity of a few meters per second. Substituting Eq. 29 into the species mass balance we get the fundamental species mass balance equation which needs to be solved with respect to the gas chemical composition at the surface:

$$J_i + y_{i,w}\dot{m}_c = w_i. \tag{30}$$

By multiplying by the species enthalpy and summing up over all species we get

$$\sum_{i=1}^{N_s}(J_i h_i) + \dot{m}_c h_w = \sum_{i=1}^{N_s} w_i h_i, \tag{31}$$

a result that will be useful shortly. Returning to the energy balance and by stating that there are no pyrolysis gases, we get

$$\begin{aligned} -\kappa_{tr}\nabla T_{tr} - \kappa_{ve}\nabla T_{ve} + \sum_{i=1}^{N_s}(J_i h_i) + \dot{m}_c h_w + q_{\text{rad,in}} = \\ -\kappa_c \nabla T + \dot{m}_c h_c + \alpha \dot{q}_{\text{rad}} - \sigma\epsilon T_w^4. \end{aligned} \tag{32}$$

A more convenient form of the energy balance can be retrieved by substituting the result of Eq. 31 into Eq. 33 to obtain

$$\begin{aligned} -\kappa_{tr}\nabla T_{tr} - \kappa_{ve}\nabla T_{ve} + \sum_{i=1}^{N_s}(w_i h_i) + q_{\text{rad,in}} = \\ -\kappa_c \nabla T + \dot{m}_c h_c + \alpha \dot{q}_{\text{rad}} - \sigma\epsilon T_w^4, \end{aligned} \tag{33}$$

where the term $\sum_{i=1}^{N_s}(w_i h_i) - \dot{m}_c h_c$ represents the enthalpy of ablation.

4. Pyrolyzing Ablating Surface

Many ablative materials, particularly those used in re-entry applications, are infused with phenolic resins, which attenuate heating since pyrolysis produces a gas mixture that blows into the boundary layer thickening it. In the most general case, the complete set of non-linear equations for energy

$$\begin{aligned} -\kappa_{tr}\nabla T_{tr} - \kappa_{ve}\nabla T_{ve} + \sum_{i=1}^{N_s}(J_i h_i) + \rho u h + q_{\text{rad,in}} = \\ -\kappa_c \nabla T + \phi \rho_{pg} h_{pg} u_{pg} + \rho_c h_c u_c + \alpha \dot{q}_{\text{rad}} - \sigma\epsilon T_w^4 \end{aligned} \tag{34}$$

and for mass

$$J_i + \rho_i u - \phi \rho_{pg,i} u_{pg} = w_i. \tag{35}$$

would have to be employed. Nonetheless, under certain assumptions simplifying approaches can help reduce the complexity of the problem (see for example [30], or steady-state ablation [31]). The complete balances for charring ablators including pyrolysis gases is currently in active development in Ares. Simplified methods consistent with the film coefficient methodology commonly used in aerospace applications is therefore used the applications presented in this work.

C. Current Implementation

The balances described above provide the generalized physical representation of the fluxes at a surface connecting a high-enthalpy gas with a pyrolyzing ablator. Depending on the specific application (e.g. CFD, material response, coupled), Ares supports different implementations and discretizations of the surface balances depending on the specific form in which they are needed by an application.

1. Fluid Boundary Conditions

Imposing boundary conditions for the CFD side through Ares can be achieved by either solving one of the surface energy balances to retrieve the surface temperature and chemical composition, or by directly imposing the already known state from the material response simulation, and then compute the necessary fluxes. More details for these two approaches are given below.

Balance equations: In the first approach taken, the complete surface energy balance, in its original form, is imposed as a boundary condition on the CFD side, where it is solved to obtain the surface temperature, coupled with the surface species mass balance. With the steady-state fluid solution converged, a net fluid to solid heat flux is calculated, which is transferred along with the local pressure to the material solver. During the time accurate integration of the material solver, an energy balance is being solved which keeps the externally imposed components of the gas-phase heat fluxes constant in time. This approach, essential due to the fact that a steady-state fluid simulation has to be coupled to a time accurate material response simulation, updates only the most important components of the surface energy balance on the material side, such as surface radiation and solid heat conduction, providing a sufficiently good approximation of the heating over the average solid solution time. The specifics of the process will be described below.

On the CFD side, the process to obtain the surface chemical composition and temperature begins with the species surface mass balances. Assuming a Fickian diffusion model and lagging the surface chemical production rate to the latest available state, the surface composition in terms of mass fractions is equal to

$$y_{s,w} = \frac{\dot{\omega}_s \delta s_f + \rho_w D y_{s,i}}{\dot{m}_c \delta s_f + \rho_w D}, \tag{36}$$

with δs_f being the distance of the first computation cell where $y_{s,i}$ was evaluated, to the surface cell center. As mentioned previously, the surface mass blowing rate can be calculated by the formula:

$$\dot{m}_c = \sum_{k=1}^{N_c} \dot{\omega}_k. \tag{37}$$

Both chemical production rates and the diffusion coefficients are a function of temperature, which is in turn given by the solution of the surface energy balance.

The surface energy balance is solved in the CFD boundary conditions for the temperature at the wall using a Newton-Raphson method, ($T_w^{n+1} = T_w^n - f/f'$), with

$$\begin{aligned} f = \frac{\kappa_{tr}}{\delta s_f}(T_i - T_w)_{tr} + \frac{\kappa_{ve}}{\delta s_f}(T_i - T_w)_{ve} + \sum_{k=1}^{N_{s,f}} \frac{\rho h_k D}{\delta s_f}(y_i - y_w)_k \\ + \alpha \dot{q}_{rad} - \dot{m}_c(h_c - h_w) + \frac{\kappa_c}{\delta s_c}(T_i - T_w)_c - \sigma \epsilon T_w^4 \end{aligned} \tag{38}$$

and an analytical Jacobian with respect to the temperature given by

$$f' = -\frac{\kappa_{tr}}{\delta s_f} - \frac{\kappa_{ve}}{\delta s_f} - \dot{m}_c(Cp_c - Cp_f) - \frac{\kappa_c}{\delta s_c} - 4\sigma\epsilon T_w^3. \tag{39}$$

Note that the diffusive fluxes are neglected in the derivative function, but could be approximated numerically with a perturbation method. Since T_w changes during the iterative process, the surface mass balances need to be re-computed, along with the surface chemistry terms. This is only not true for models that are not temperature dependent or for scenarios of steady-state ablation.

A converged surface state, imposed also by the convergence of the global CFD calculation, allows for the calculation of the net, CFD heat flux which will be passed to the material solver. In this approach, the net heat flux is equal to

$$\begin{aligned} q_{\text{net, CFD}} &= \frac{\kappa_{tr}}{\delta s_f}(T_i - T_w)_{tr} + \frac{\kappa_{ve}}{\delta s_f}(T_i - T_w)_{ve} \\ &+ \sum_{k=1}^{N_{s,f}} \rho h_k D(y_i - y_w)_k + \dot{m}(h_c - h_w) + \alpha \dot{q}_{rad}. \end{aligned} \tag{40}$$

Note that the net heat flux as computed from CFD is not the complete one applied to the material response boundary condition, since an additional surface energy balance is internally solved. The rest of the components, not appearing in the equation above, but existing in the global surface energy balance, are updated in a time accurate manner in the material solver and will be discussed in more details in a following section. While the exact choice of which term to include one each phase can be to some extent arbitrary, attention should be paid to keeping the approach consistent and conservative. More details will be presented when the material response boundary conditions are discussed.

Fixed State: An alternative to solving the complete surface energy balances on the CFD side until convergence is reached is to directly return from the material response code the surface temperature as calculated from the material solver. This approach, apart from being significantly simpler, enforces consistency and continuity of the boundary conditions at the beginning of each material response solve for the two phases, even though the imposed temperature is the result of an approximation of the surface energy balance. In summary, for this approach, the net heat flux is computed from Eq. 40 as before, and T_w is determined by the energy balance of the material response solver, with the rest of process remaining the same.

2. Material Response Boundary Conditions

As mentioned above, the material response code takes a direct flux from the CFD and solves an approximate energy balance for the surface temperature. This balance includes only the solid conduction and surface radiation terms

$$-\frac{\kappa_c}{\delta s_c}(T_w - T_i) = q_{\text{net,CFD}} - \sigma\epsilon T_w^4. \tag{41}$$

It is worth noting that this approximation assumes that the effects of any temperature changes during the solid solve do not significantly affect the gas-surface interaction chemistry and the former's effect on heating. This approximation may not be accurate during periods of significant surface temperature changes or during periods where shape change significantly alters the aerothermal environment. From a practical stand-point this means that the allowable decoupling of time-scales is dependent on the transience of the surface phenomena and the rate of shape change.

3. Approximations for Pyrolyzing Ablators

If pyrolysis gas blowing is assumed absent from the surface energy and mass balances (and in the flow field), an approximate method can be derived from film coefficient theory. This assumption is useful since the inclusion of pyrolysis gas blowing requires introducing a large number of additional gas species into the flow, which increases the computational complexity by expanding the number of species conservation equations and requiring a more complicated set of chemical kinetics. At the surface, pyrolysis gases affect heating through blowing (advection of gases away from the surface) that results in boundary layer thickening thereby reducing heating and through chemical shielding of the surface. The pyrolysis byproducts entering the boundary layer can inhibit atomic species such as oxygen and nitrogen from reaching the surface and reacting exothermically. In the standard uncoupled approach these mechanisms are approximated through a blowing correction and advection energetics in the energy balance. A common boundary condition for this type of approach, known as the *aeroheating boundary condition*, has the following form

$$-\kappa\nabla T_c = C_H^*(h_r - h_w) + \dot{m}_c h_c + \dot{m}_{pg} h_{pg} - \dot{m}_w h_w - \sigma\epsilon T_w^4, \tag{42}$$

where

$$\dot{m}_w = \dot{m}_c + \dot{m}_{pg}, \tag{43}$$

where h_r is the recovery enthalpy, and C_H^* is the corrected film coefficient. The film coefficient blowing correction [32] has historically been applied from

$$C_H^* = C_H \Omega \tag{44}$$

where C_H is the unblown film coefficient derived from CFD, and

$$\Omega = \frac{\Phi}{e^{\Phi} - 1} \tag{45}$$

where

$$\Phi = \frac{2\lambda \dot{m}_w}{C_H}, \tag{46}$$

here λ is a phenomenological coefficient that is typically set to $\lambda = 0.5$ for laminar and $\lambda = 0.4$ for turbulent flows.
In Ares, two methodologies are available for approximating the pyrolysis gas contribution. The first is to apply the aeroheating boundary condition almost identically to an uncoupled procedure, except that the film coefficient is recomputed as the heat flux varies due to temperature changes. This is similar to applying a hot wall correction to the film coefficient, however it is not phenomenological in nature. This boundary condition is most useful when the surface phenomena is mostly steady, but changes in shape due to recession can affect heating profiles. The second approach is to leverage information available from the coupling interface and approximate the pyrolysis contribution to the energy balance. The energy balance solved in material response becomes

$$-\kappa \nabla T_c = q_{\text{net,CFD}} + \dot{m}_{pg}(h_{pg} - h_w) - \sigma \epsilon T_w^4 \tag{47}$$

where $q_{\text{net,CFD}}$ is obtained by solving Eq. 40 either through an energy balance in the flow solver or through fixed state approach. This approximation assumes that the pyrolysis products injected in the boundary layer do not interact with the products of the carbon ablation processes neither chemically nor through diffusion. Finally, while $\dot{m}_c$ can be computed via a finite-rate ablation model or a B' model, $\dot{m}_{pg}$ is defined as

$$\dot{m}_{pg} = \phi \rho_{pg} u_{pg} \tag{48}$$

where u_{pg} is a solution to the porous transport. In this work, it is computed using Darcy's Law [33]

$$u_{pg} = -\frac{K}{\phi \mu} \nabla P \tag{49}$$

where K is material permeability, and μ is the gas viscosity, which along with h_{pg} is defined based on chemical equilibrium pyrolysis gas thermodynamic and transport properties databases [34, 35].

D. Surface Chemistry

There are several finite-rate ablation models for the air-carbon system [36–39] which have been implemented in coupling frameworks [34, 40–43]. A recent model, developed by Prata et al. [44], known as the ACA model, derives rates of reaction on data from molecular beam experiments by Murray et al. [45, 46]. The model is implemented in this work and is a 20-reaction model with O, O_2 and N reactants. Every reaction depends on the surface coverage of the reactants, [O(st)], [O*(st)], and [N(st)] and the surface density of empty sites [(st)], where the initial total density of active sites is $B = 1 \times 10^{-5}$ mol m^{-2}, as used in the previous studies from Poovathingal et al. [38, 39] and Zhluktov-Abe [37]. Once all the reaction rate coefficients are computed at the wall temperature, a system of ordinary differential equations (ODEs) is assembled where the reaction rates are computed for each mechanism, and the production rate of each species is updated. Finally, the density of empty surface sites is computed knowing that

$$[(st)] = B - [O(st)] - [O^*(st)] - [N(st)]. \tag{50}$$

Once the density of empty surface sites reaches steady-state, the species mass fluxes, in kg/m^2, are computed from

$$\dot{w}_s = f_{[s]} M_s \tag{51}$$

where $f_{[s]}$ is the molar flux of species s at the surface given by

$$f_s = \frac{d[s]}{dt} \tag{52}$$

where $[s]$ is the molar concentration of species s in units of mol/m^2. The table of reaction rates and the specific system of ODEs solved is described in Prata et al. [44]. Carbon sublimation reactions are also modeled for C, C_2, C_3 based on the rates from Keenan et al. [47–50].

VI. Coupled Mesh Motion

A. Primer on Mesh Motion Algorithms

For structured, single block grids, simple algebraic relations can be used as mappings for the node displacements by using interpolation along grid lines between surface definitions [51]. These methods are very efficient, however, for complex geometries and multiple materials, unstructured, multi-block grids may be needed. One commonly used mesh motion method is the spring analogy [52]. Here springs are used as analogies for grid connectivity where displacements are applied based on stiffness associated with length of connections. These methods can be used on structured and unstructured meshes but can lead to tangling [53] and cell inversion [54]. Furthermore, this approach can be expensive. A different class of methods uses solutions to partial differential equations by augmenting the system of equations to include dynamics [55]. Common implementations of these methods include solving a set of elliptic followed by bi-harmonic equations to preserve wall orthogonality [56]. The PDE-based methods suffer from some of the same drawbacks of spring analogy where mesh quality is not guaranteed, and they can be computationally expensive. The last class of methods are powered by interpolation [57, 58]. These are desirable because they are robust and connectivity free. This work focuses on one interpolation methodology based on radial basis functions [59, 60].

B. Current Implementation

The algorithm for moving the computational meshes applied is described in detail in Section IV as it is also used for the interpolation of data at the boundary. The key differences when applying the RBF interpolation to the movement of the mesh is in the selection of basis function and in what constitutes as source and target data. In the context of moving computational meshes, the primary concerns are that the operations preserve grid quality by minimizing cell or face metric deterioration such as skewness, aspect ratio, taper, torsion, and stretch, and that the displacement field applied at the boundaries be accurately reconstructed after the interpolation step. As explained in Section IV, compact basis functions have desirable properties both in their behavior as well as in the sparsity they add to the linear system that must be solved. Wendland functions [58], shown in Table 1, are particularly well suited to mesh motion applications due to their their smoothness properties and the sparsity they provide. Figure 7a shows the form of various ordered

Table 1 Wendland radial basis functions.

Name	Basis Function
Wendland-C0	$(1-r)^2$
Wendland-C2	$(1-r)^4(4r+1)$
Wendland-C4	$(1-r)^6(35r^2+18r+3)$
Wendland-C6	$(1-r)^8(32r^3+25r^2+8r+1)$

Wendland functions with respect to distance between a source and target point and Fig. 7b shows the effect of base radius selection on the displacement curve. Effectively, large base radii spread the displacement over larger distances in the mesh providing higher smoothness, however, this decreases sparsity which becomes a trade-off. The error associated with the reconstruction of a displaced surface relates to how the displacement vectors, which are face-based quantities, are reconstructed at the boundary nodes of a grid. The simplest implementation of the RBF method would include the boundary nodes in the solution vector, using the boundary faces as source points. However, it was found that this methodology accrued significant error for large aspect ratio cells (if the distance from the face center to the nodes approached the base radius). Figure 8 illustrates this point as it shows the error on a 1-dimensional "bar" as a function of

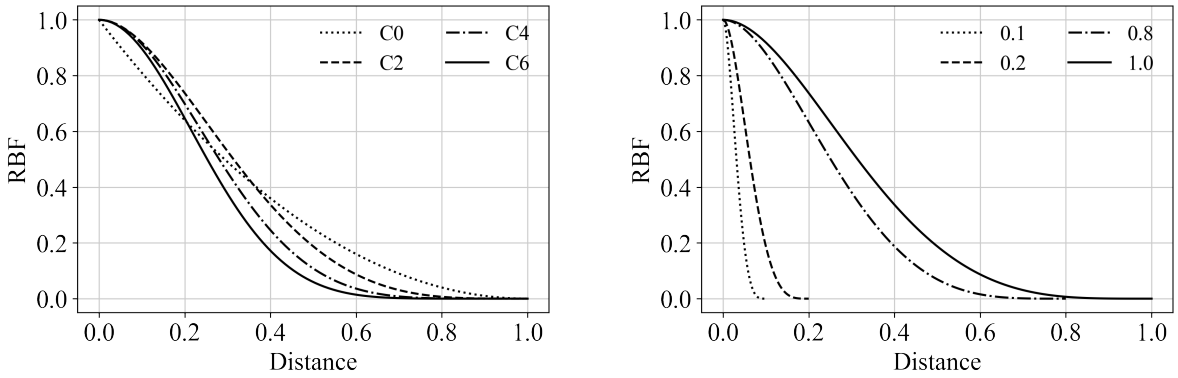

(a) Compact support Wendland functions.

(b) Effect of base radius.

Fig. 7 Radial basis functions.

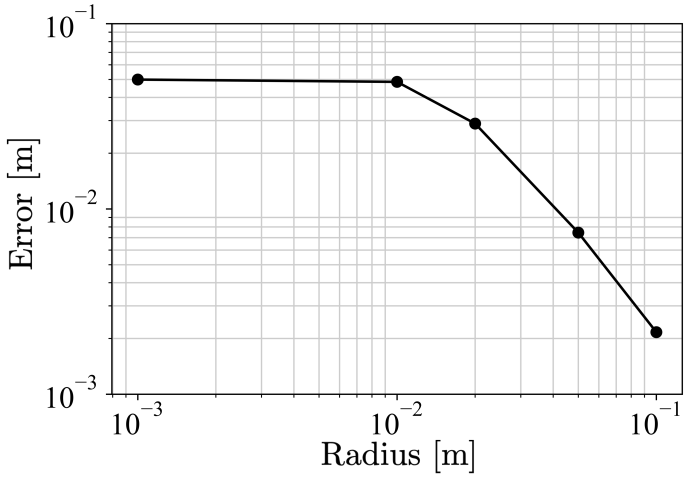

Fig. 8 Error on 1-dimensional "bar" with face-based source point.

base radius when the face-center of the ablating boundary (a single face) is used as the source point. A better selection of source points is the boundary nodes, which enforces the displacement condition exactly. The displacement at the nodes is computed via inverse weighted distance from a node to all connected boundary faces. This point is illustrated by applying an analytical displacement field to a 2-dimensional surface of a 3-dimensional cube using the Gaussian distribution,

$$\Delta s(x, y) = \frac{1}{2\pi\sigma^2} \exp - \frac{x^2 + y^2}{2\sigma^2} \tag{53}$$

where $\sigma = 0.3$. Figure 9 shows the computational set-up. The error between the analytical and nodal displacement is shown in Fig. 10 using face-based (Fig. 10a) and node-based (Fig. 10b) source points. It is shown that node-based source points have significantly lower error than face-based.

C. Coupling Context

The mesh motion step can be one of the most expensive portions of a simulation; therefore, it is desirable to reduce the cost of the operation either by leveraging information from one domain and re-using it for the other, or by performing only one mesh motion solve for both domains. In this work the former approach has been implemented whereby only one linear system solve is necessary. The system is sized by the number of source mesh points at the material response ablating boundary. In order to do this, it is assumed that the source points of the material response solver provide a

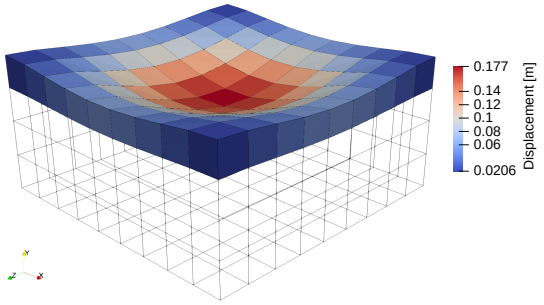

Fig. 9 Gaussian displacement field.

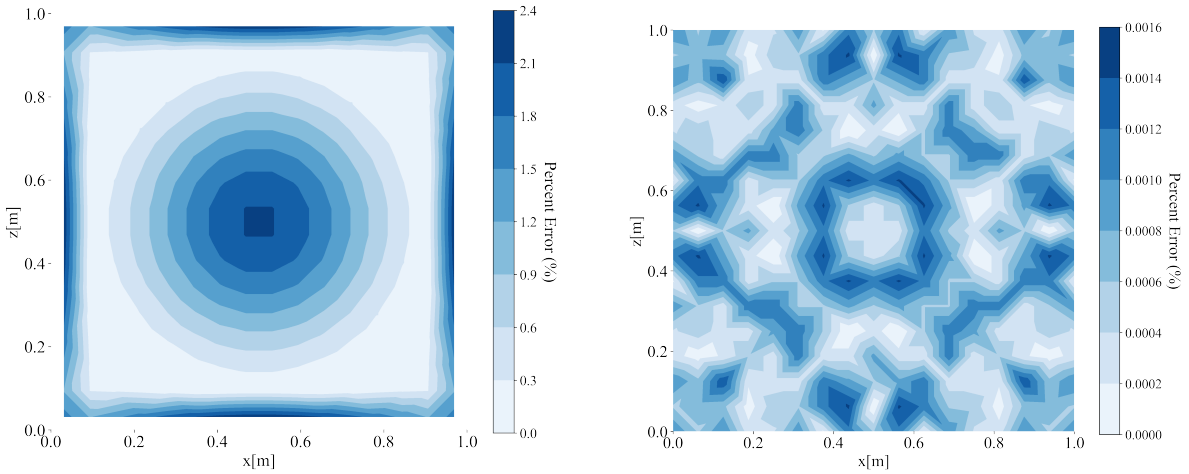

(a) Face-based source points. **(b) Node-based source points.**

Fig. 10 Displacement error on the surface of a cube.

sufficiently resolved boundary on the flow solver side. In practice this means that a sufficiently large base radius needs to be used in order to accurately represent the displacement vector of a material response face to a CFD face.
The linear system is solved as described in Eq. 3. The α values computed based on the material response surface are then used to solve Eq. 6 for both the material response grid and the CFD grids. Figure 11a shows the recessed shapes of an Iso-Q geometry exposed to arc-jet flow. It is notable that coupling the shape change has a large impact on the regions with curved features (the shoulder in this case) as these play a significant role in the spatial distribution of the heating, as shown in Fig. 11b.

VII. Simulation of a Shear Test Article in Arc-Jet Flow

To assess the merit of the developed methodology in a fully-coupled context, a complex configuration is simulated which stress tests many of the components of the framework. A shear test article in arc-jet environment is selected for the variety of participating phenomena that are highly coupled. The following are a few of the aspects of the configuration that add complexity to the simulation:

- Significant shape change;
- Multi-material;
- Multiple coupled zones, with ablating/non-ablating interfaces;
- Gas-surface interaction chemistry;
- High-enthalpy/high heating conditions;
- Multi-dimensional (surface phenomena is not iso-q);
- Anisotropic material, with angled material property orientation.

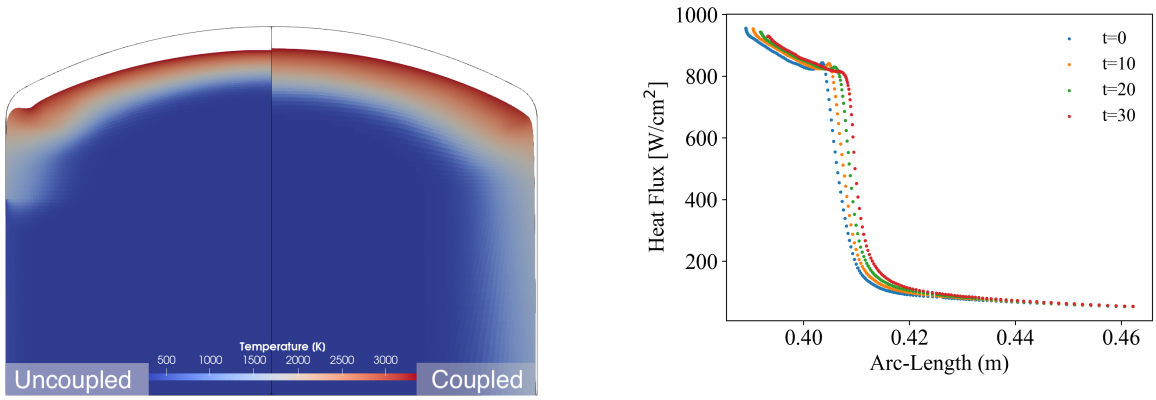

(a) Final recessed shapes. **(b) Heating profile.**

Fig. 11 Effect of coupling on shape change of an IsoQ.

The particular configuration simulated in this chapter has been modeled previously by Driver et al. [61] and [21]. The case is based on the experimental conditions of the Mars Science Laboratory high shear test campaign [62].

A. Test Conditions and Diagnostics

A shear test was performed on a wedge article in the 60 MW Interactive Heating Facility (IHF) arc-jet at NASA Ames Research Center. Figures 12a and 12c show the pre- and post-test sample of FiberForm, respectively. The test conditions were facility max, with 6000 amp arc current, and a mass flow rate of 0.85 kg/s through a 6-inch nozzle. A 20° half-angle wedge was placed downstream of the nozzle exit. The exposure time of the test was 21 seconds. The test article consisted of a copper holder with water-cooled cylinders near the stagnation region and a sample of FiberForm. Recession was measured via post-test sample analysis and recorded. It is worth noting that visible streaks of ablated material appeared at various spanwise locations, the peaks and valleys of these streaks give an interval of recession values with the difference between these being approximately 1 mm in the region of maximum difference.

(a) Pre-test wedge article.

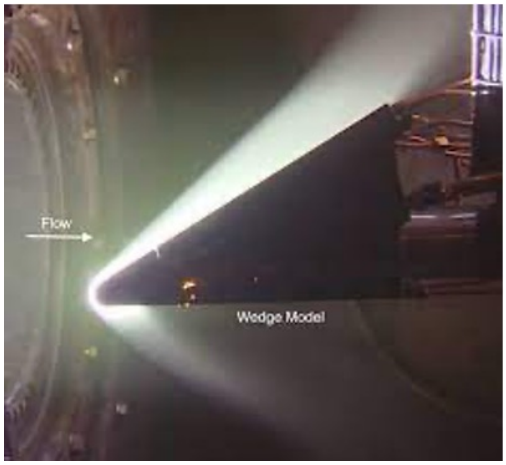

(b) Arc-jet flow over wedge article.

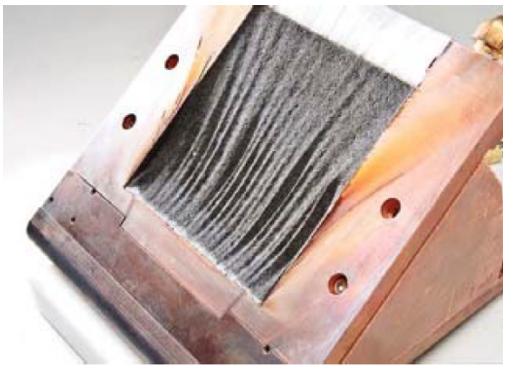

(c) Post-test wedge article.

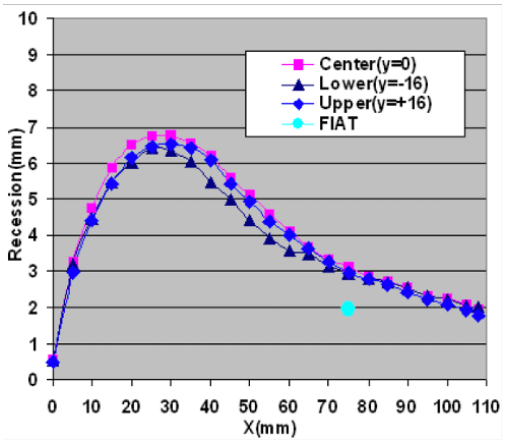

(d) Measured recession on the ablated sample.

Fig. 12 Experimental set-up and collected data, from Driver et al. [61].

B. Flow Set-Up

The fluid domain is modeled from an interpolated solution of a full nozzle and vacuum chamber at the conditions specified in Sec. VII.A. A smaller domain, localized to the sample, was generated in order to reduce computational cost since the phenomena local to the sample surface has virtually no effect on the nozzle flow or pre-shock region.The inflow conditions for the subdomain are shown in Table 2.

Variable	Value	Units
ρ	0.00671	kg/s
u	4818.0	m/s
T_{tr}	4744.0	K
T_{ve}	4535.0	K
y_{N_2}	0.5107	-
y_{NO}	0.0006	-
y_N	0.2079	-
y_O	0.2172	-
y_{Ar}	0.0636	-
$T_{w,i}$	300.0	K

Table 2 Fluid simulation conditions.

Two wall boundary condition types are employed. The copper boundary is modeled through a non-ablating, coupled boundary condition, in which a surface energy balance of convective and re-radiative heat transfer is solved. It is worth noting that catalytic reactions are not modeled on this boundary, which can lead to a difference in the species that diffuse downstream to the ablating sample thereby affecting the surface chemistry there. The sample boundary employs a fully coupled surface energy balance with the finite-rate chemistry ACA model described in Sec. V.D.

C. Material Response Set-Up

The material domain consists of a 2-dimensional extrusion of a slice across the center of the wedge. Two material zones are modeled: the copper holder and the FiberForm sample. The solid computational grid is comprised of two volume zones, the sample zone has 1856 hexahedral cells, while the copper zone uses 11002 cells with a mixture of hexahedral and triangular prism elements. The copper holder contains three cooling cylinders, which are modeled as isothermal boundaries with a temperature of 300K. The sample surface is treated as a moving boundary with source points being set at node-center locations. The base radius for the RBF interpolation is 8 mm. The FiberForm sample is modeled by rotating the anisotropic material properties to align with the wedge angle (70° rotation). Icarus solves for the material response using a backward-Euler, implicit time-integration scheme and a least-squares gradient reconstruction scheme. GMRES is used to solve the linear system. Figure 13 depicts the computational setup of the solid.

D. Results

Figure 14 shows the coupled fluid and solid solutions after $5, 10, 15, 21$ seconds of exposure time. On the solid side, one can note the increase in temperature over time due to thermal conduction. The copper, having a high thermal conductivity, quickly conducts heat through the entire depth of the holder. Notably, the cooling cylinders near the stagnation region of the article prevent the high heating from the stagnation region from penetrating the article. The FiberForm sample incurs significantly higher temperatures from low thermal conductivity, but prevents the heat front from reaching the bondline for a significant amount of time. As time advances, one can start noting the change in shape of the sample due to ablation. As this occurs, the region near the sample interface begins to cool, and the higher heating portion moves downstream. Finally, at the last time-stamp, 21 seconds, one can note that the sample begins to cool. This appears to be due to the flow separation. On the fluid side, one can observe the expansion fan that forms at the interface where the sample begins to ablate. After significant ablation, a backward-facing step feature is formed, and the flow separates and re-attaches further downstream. This reduces the heating near the step and creates a re-circulation region. After 21 seconds the fast moving flow no longer reaches the surface, and the sample stops ablating and begins to

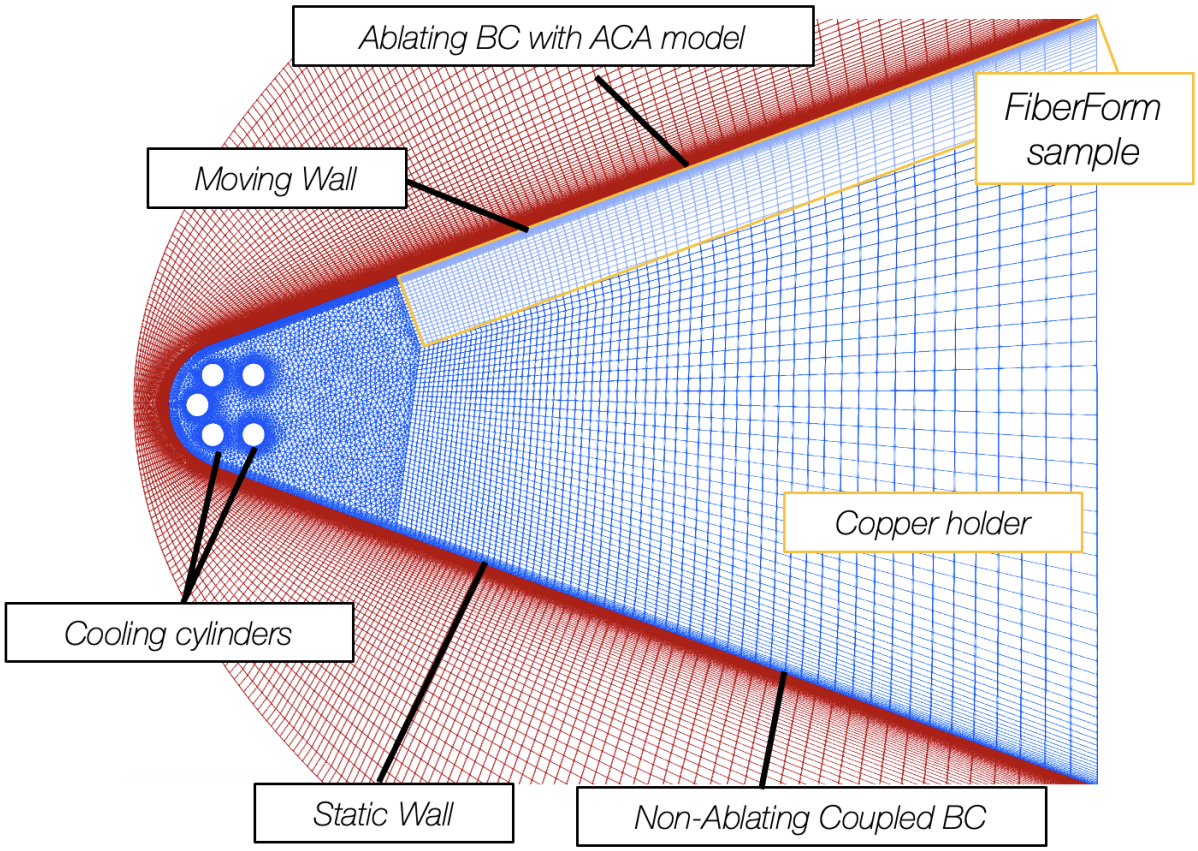

Fig. 13 Solid computational set-up.

cool. There are two explanations for this. First, as previously described, flow separation reduces heating, the surface cools, and thus the ablation rates reduce. A second argument, however, can be made based on the chemical kinetics occurring withing the boundary layer. Figure 15a shows that CO accumulates in the separated flow region, and this could be shielding the surface from atomic oxygen, preventing further ablation through oxidation.

Figure 15 presents the carbonaceous species produced from ablative processes. The dominant species produced is CO, followed by CO_2. It is worth noting that the carbon products are present mostly downstream of the interface, with the exception of CO, which is present in both regions. After 21 seconds, one can notice a higher mass fraction of ablation products, notably CO mass fraction (Fig. 15a) and CO_2 (Fig. 15b). The mass fractions of CN and C (Figs. 15c,15d) are low since the surface temperature is not high enough for sublimation reactions to be dominant, and furthermore CN has a low probability of formation per the ACA model. The total surface recession of the sample is shown in Fig. 16 and compared with measured data and results from literature. It is worth noting that the approach from Driver et al., as well as that of FIAT, differ from the current work in several aspects. Any agreement between Ares and these methodologies is not expected. The maximum error (peak-to-peak) of total recession is approximately 15% with the current approach, in contrast with an error of approximately 30% from Driver et al. and 68% from FIAT. Note that this maximum error occurs near the step formation in the sample, an area in which the physical mechanisms are heavily determined by the shape of the surface. This explains the discrepancy between the FIAT solution and the current work. In the FIAT approach, the surface does not change shape due to ablation and thus the profile of recession does not change from the initial trend (does not evolve in time). Another notable difference is that the FIAT approach utilizes a different boundary condition which is based on the B′ curve and the mass/heat diffusion analogy. Thus, not only is the shape of the recession curve expected to be different but also the magnitude, which is associated with the gas-surface interaction model. In the work of Driver et al., the shape change is accounted for, but the conduction to the material is neglected. Additionally, the gas-surface reactions are modelled differently in that only carbon oxidation to produce

CO and catalysis of N and O were considered. Furthermore, the reaction rates were based on a user-input γ model. Overall, the difference in total recession between the Ares prediction and the measured values are still significant. Future analysis should include 3-dimensional simulations whereby the effects of vortex formation, which increase mixing of atomic species to the surface and heating, can be accounted for. Those effects would likely increase the total recession. Figure 17 shows the surface quantities as they evolve over time, and the transient nature of this problem is highlighted. It is clear that the changing shape of the surface has a large effect on heating and thereby recession rates.

Figure 18 shows the mass fractions of species at the surface at 0.5 seconds. One can observe from Fig. 18a that CO production drives ablation, followed by CO_2 at an order of magnitude lower, and C and CN at three and four orders of magnitude lower, respectively. Figure 18b suggests that atomic oxygen is significantly more likely to produce a carbon bearing product than to recombine and produce molecular oxygen. Finally, Fig. 18c suggests the opposite trend is true for atomic nitrogen, where recombination is significantly stronger than formation of CN at these conditions.

VIII. Conclusion

This work focused on the development of a framework for multi-physics modeling. A novel approach using API to manage physics kernels with a high degree of flexibility, allowing for detailed exchanges of information was implemented. Radial basis function interpolation methodology is used for reconstructing arbitrary boundary data on opposing sides of an interface and for mesh motion.

The physical phenomena that is responsible for driving the coupled behavior in ablation occurs at the surface and is fundamentally a process of mass and energy transfer. The methodology and implementation of coupled boundary conditions is described in this work and is employed for modeling surface chemistry.

Finally, a shear test article in an arc-jet flow is simulated using the developed framework. The complexity of the configuration, including non-trivial shape change induced by gas-surface interaction chemistry, multi-material set-up with distinct coupling boundary conditions, and relatively long exposure time, demonstrate multi-physics capabilities of the solver. The results of the current framework are compared with literature and are shown to provide a significant improvement to the predicted total recession of the material sample.

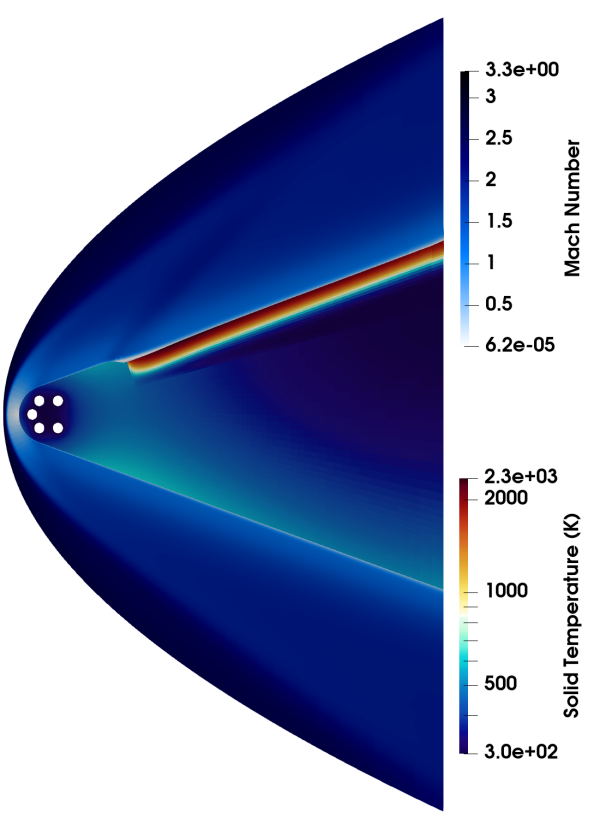

(a) 5 seconds.

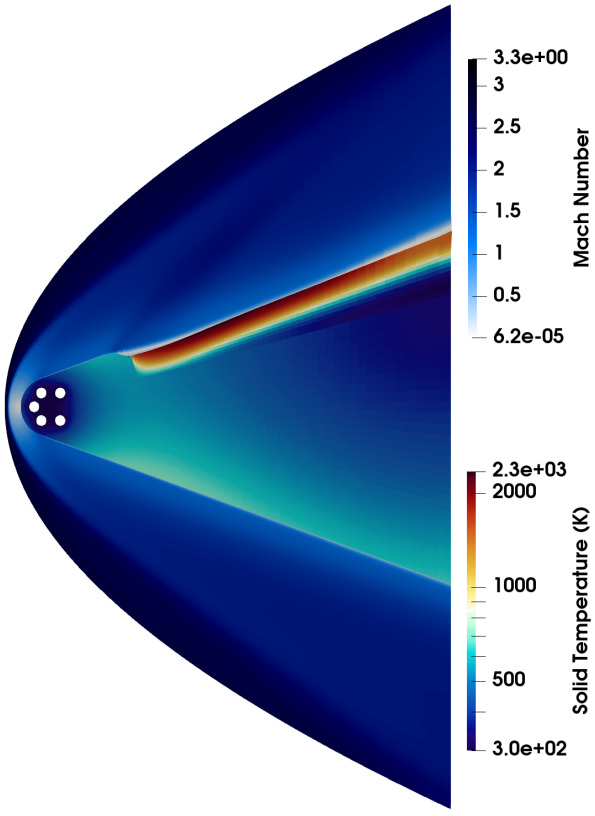

(b) 10 seconds.

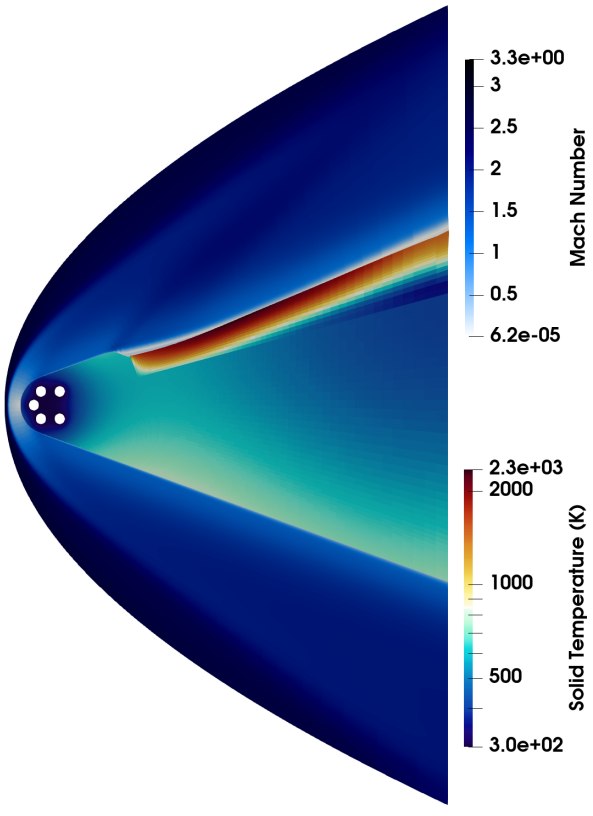

(c) 15 seconds.

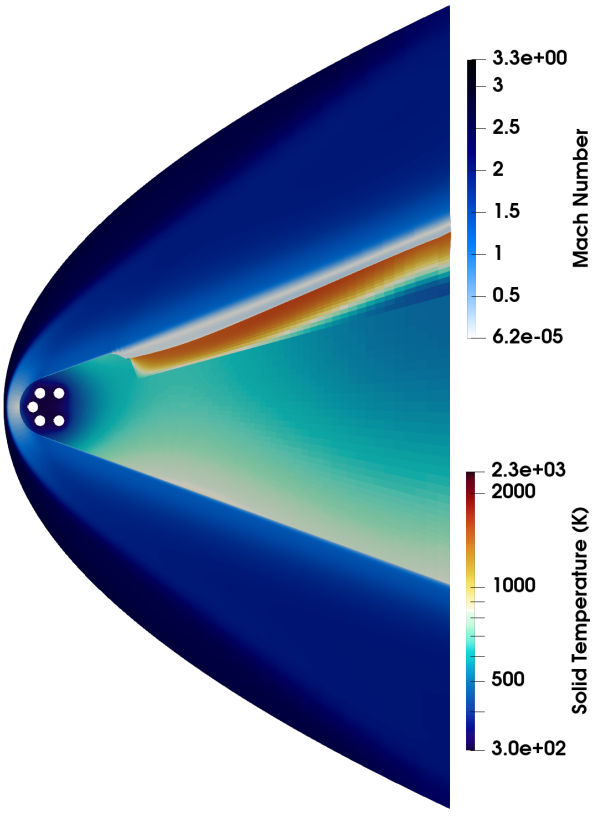

(d) 21 seconds.

Fig. 14 Snapshot of the flow and material at various time stamps.

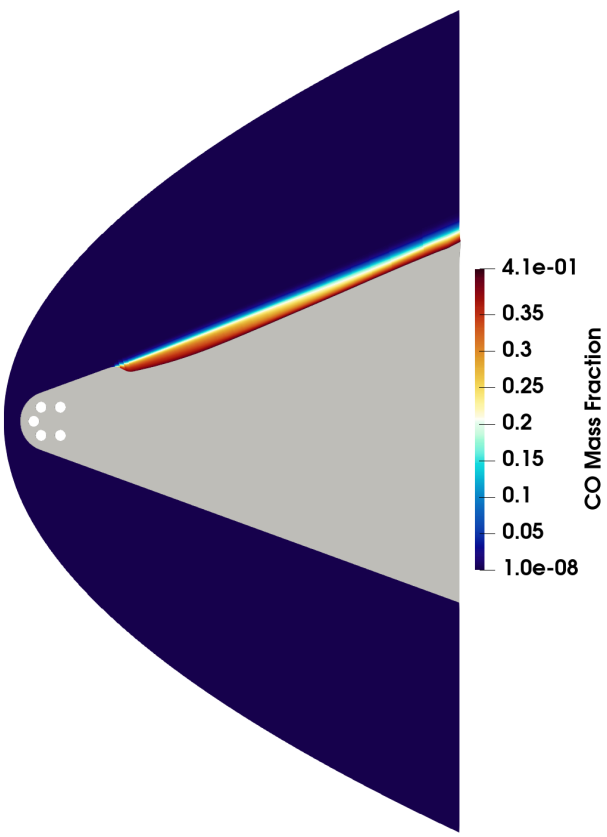

(a) CO.

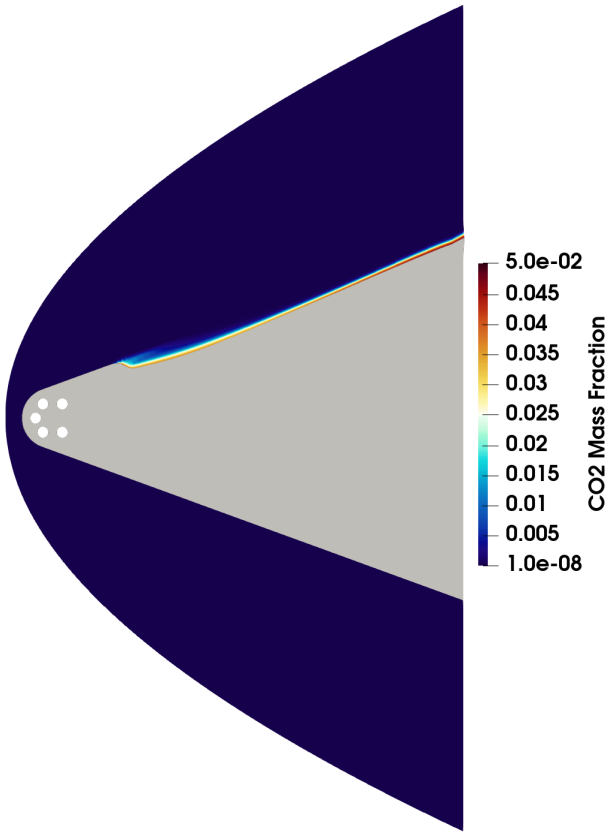

(b) CO_2.

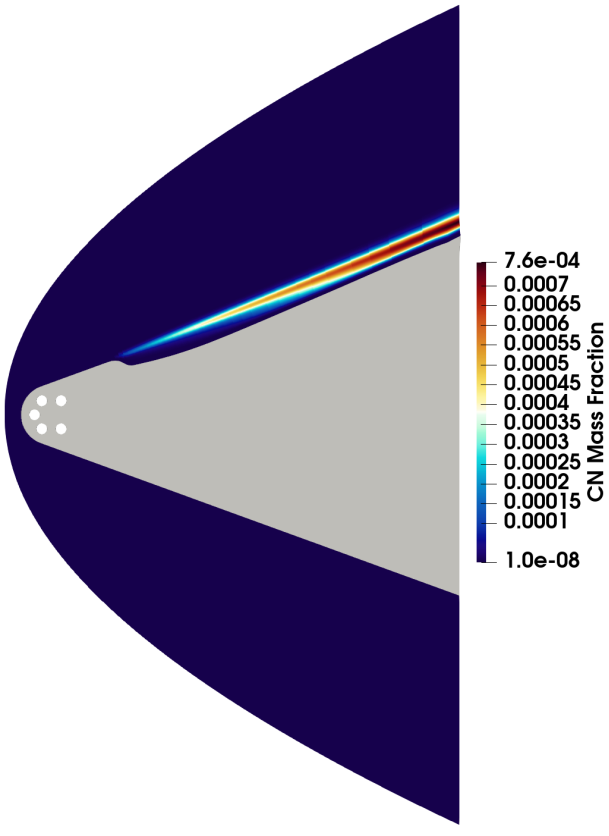

(c) CN.

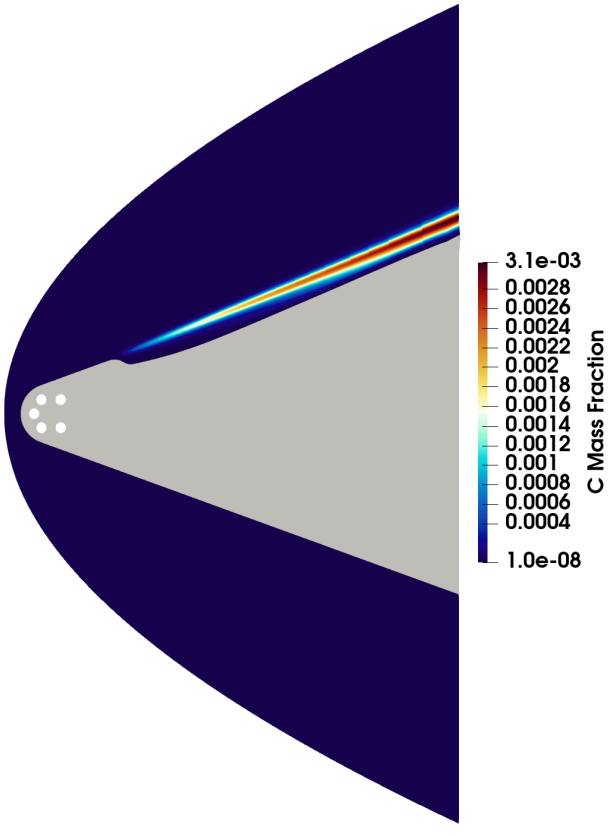

(d) C.

Fig. 15 Carbon species mass fraction after 21 **seconds.**

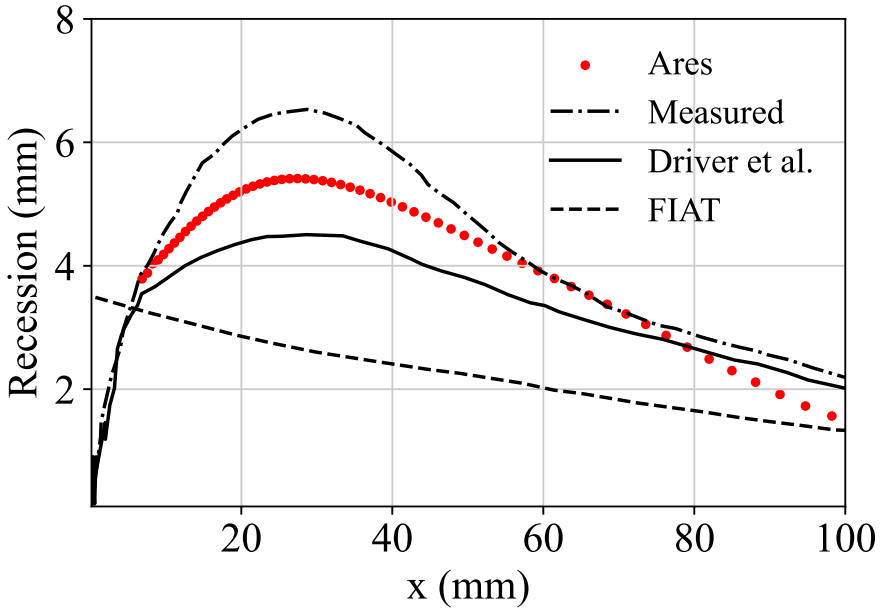

Fig. 16 Total recession on shear article after 21 **seconds.**

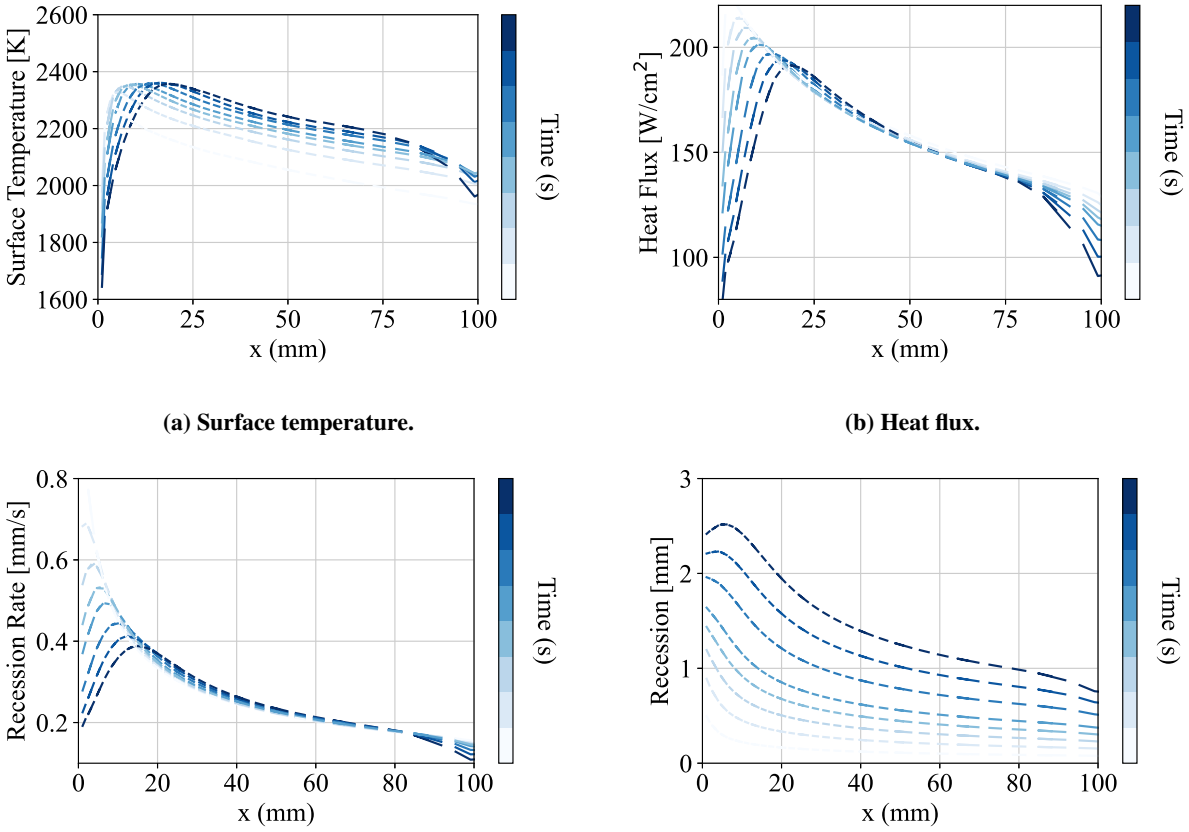

(a) Surface temperature.

(b) Heat flux.

(c) Recession rate.

(d) Surface recession.

Fig. 17 Surface quantities through time, from 0.5 **to** 5 **seconds.**

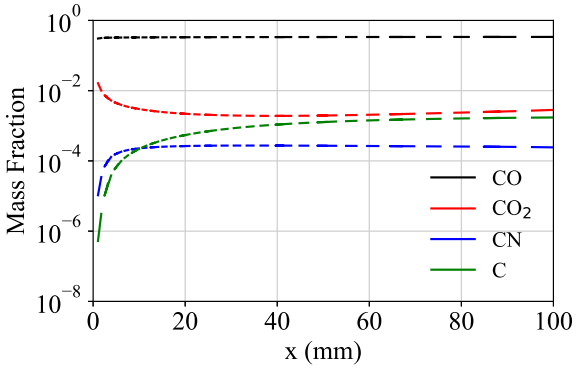

(a) Carbon bearing species.

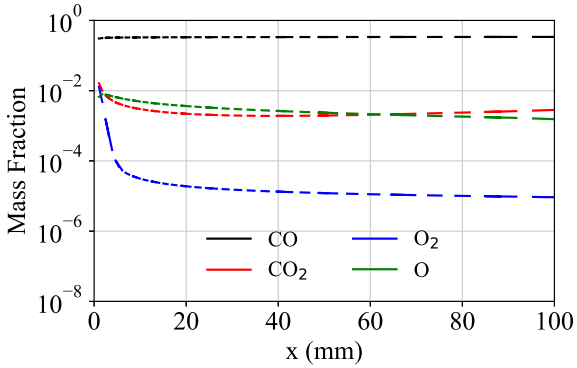

(b) Oxygen bearing species.

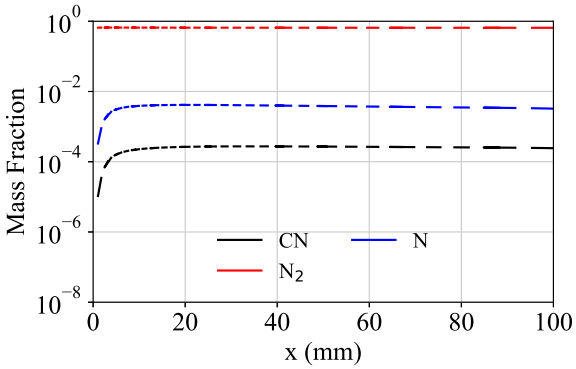

(c) Nitrogen bearing species.

Fig. 18 Mass fractions at the surface.

Acknowledgments

The primary author of this work is funded by the Entry Systems Modeling Project (ESM) and the Mars Sample Return Earth Entry System (MSR-EES) project. This work was funded by the NASA Space Technology Graduate Research Opportunities (NSTGRO) under grant number 80NSSC18K1150 and the NASA Space Technology Research Institute Advanced Computational Center for Entry System Simulation (ACCESS).

References

[1] Nompelis, I., Drayna, T., and Candler, G., "A Parallel Unstructured Implicit Solver for Hypersonic Reacting Flow Simulation," *AIAA 2005-4867*, 2005. https://doi.org/10.2514/6.2005-4867.

[2] Nompelis, I., Drayna, T., and Candler, G., "Development of a Hybrid Unstructured Implicit Solver for the Simulation of Reacting Flows Over Complex Geometries," *AIAA 2004-2227*, 2004. https://doi.org/10.2514/6.2004-2227.

[3] Candler, G. V., Johnson, H. B., Nompelis, I., Gidzak, V. M., Subbareddy, P. K., and Barnhardt, M., "Development of the US3D Code for Advanced Compressible and Reacting Flow Simulations," *AIAA 2015-1893*, 2015. https://doi.org/10.2514/6.2015-1893.

[4] Schulz, J. C., Stern, E., Muppidi, S., Palmer, G., Schroeder, O., and Martin, A., "Development of a three-dimensional, unstructured material response design tool," *AIAA 2017-0667*, 2017. https://doi.org/10.2514/6.2017-0667.

[5] Sahai, A., and Johnston, C. O., "On Computationally Efficient Radiative Transfer Calculations for Three-dimensional Entry Problems," *AIAA Paper 2023-0204*, 2023. https://doi.org/10.2514/6.2023-0204.

[6] Sahai, A., Johnston, C. O., Lopez, B., and Panesi, M., "Comparative analysis of reduced-order spectral models and grouping strategies for non-equilibrium radiation," *Jounral of Quantitative Spectroscopy and Radiative Transfer*, Vol. 242, 2019. https://doi.org/10.1016/j.jqsrt.2019.106752.

[7] Chen, Y. K., and Gökçen, T., "Implicit Coupling Approach for Simulation of Charring Carbon Ablators," *Journal of Spacecraft and Rockets*, Vol. 51, No. 3, 2014.

[8] Farhat, C., Lesoinne, M., and Tallec, P. L., "Load and motion transfer algorithms for fluid/structure interaction problems with non-matching discrete interfaces: momentum and energy conservation, optimal discretization and application to aeroelasticity," *Computer methods in applied mechanics and engineering*, Vol. 157, No. 1-2, 1998. https://doi.org/10.1016/S0045-7825(97)00216-8.

[9] Reinert, J. D., "Conjugate Heat Transfer Simulations for Hypersonic Vehicles," Ph.D. thesis, University of Minnesota, August 2020.

[10] Sutherland, I. E., and Hodgman, G. W., "Reentrant polygon clipping," *Communications of the ACM*, Vol. 17, No. 1, 1974. https://doi.org/10.1145/360767.360802.

[11] Franke, R., "Scattered Data Interpolation: Tests of Some Methods," *Mathematics of Computation*, Vol. 38, No. 157, 1982. https://doi.org/10.2307/2007474.

[12] Rendell, T., and Allen, C. B., "Efficient mesh motion using radial basis functions with data reduction algorithms," *Journal of Computational Physics*, , No. 228, 2009, pp. 6231–6249. https://doi.org/10.1016/j.jcp.2009.05.013.

[13] Balay, S., Abhyankar, S., Adams, M. F., Benson, S., Brown, J., Brune, P., Buschelman, K., Constantinescu, E., Dalcin, L., Dener, A., Eijkhout, V., Faibussowitsch, J., Gropp, W. D., Hapla, V., Isaac, T., Jolivet, P., Karpeev, D., Kaushik, D., Knepley, M. G., Kong, F., Kruger, S., May, D. A., McInnes, L. C., Mills, R. T., Mitchell, L., Munson, T., Roman, J. E., Rupp, K., Sanan, P., Sarich, J., Smith, B. F., Zampini, S., Zhang, H., Zhang, H., and Zhang, J., "PETSc/TAO Users Manual," Tech. Rep. ANL-21/39 - Revision 3.20, Argonne National Laboratory, 2023. https://doi.org/10.2172/1968587.

[14] Runge, C., "Über empirische Funktionen und die Interpolation zwischen äquidistanten Ordinaten," *Zeitschrift für Mathematik und Physik*, Vol. 46, 1901.

[15] Dias, B., Zibitsker, A. L., Meurisse, J. B., and Mansour, N. N., "Towards a flow-material unified solver for heatshield modeling," *AIAA Paper 2023-2718*, 2023. https://doi.org/10.2514/6.2023-2718.

[16] Duzel, U., and Martin, A., "Modeling High Velocity Flow Through Porous Media," *AIAA Paper 2020-0486*, 2020. https://doi.org/10.2514/6.2020-0486.

[17] Schrooyen, P., Hillewaert, K., Magin, T. E., and Chatelain, P., "Fully implicit Discontinuous Galerkin solver to study surface and volume ablation competition in atmospheric entry flows," *International Journal of Heat and Mass Transfer*, Vol. 103, No. Supplement C, 2016, pp. 108 – 124. https://doi.org/10.1016/j.ijheatmasstransfer.2016.07.022.

[18] Thornton, J. M., Prabhu, D. K., Meurisse, J. B., Borner, A., Monk, J. D., and Cruden, B. A., "Coupling Heatshield Response and Aerothermal Environment for Mars Entry via Surface Gas Blowing," *AIAA Paper 2023-0963*, 2023. https://doi.org/10.2514/6.2023-0963.

[19] Martin, A., and Boyd, I. D., "Strongly Coupled Computation of Material Response and Nonequilibrium Flow for Hypersonic Ablation," *Journal of Spacecraft and Rockets*, Vol. 25, No. 3, 2015. https://doi.org/10.2514/1.A32847.

[20] Kuntz, D. W., Hassan, B., and Potter, D. L., "Predictions of Ablating Hypersonic Vehicles Using an Iterative Coupled Fluid/Thermal Approach," *Jounral of Thermophysics and Heat Transfer*, Vol. 15, No. 2, 2001. https://doi.org/10.2514/2.6594.

[21] MacLean, M., Marschall, J., and Driver, D. M., "Finite-Rate Surface Chemistry Model, II: Coupling to Viscous Navier-Stokes Code," *AIAA Paper 2011-3784*, 2011. https://doi.org/10.2514/6.2011-3784.

[22] Chen, Y.-K., and Gökçen, T., "Implicit coupling approach for simulation of charring carbon ablators," *Journal of Spacecraft and Rockets*, Vol. 51, No. 3, 2014, pp. 779–788. https://doi.org/10.2514/1.A32753.

[23] Milos, F., and Rasky, D., "Review of Numerical Procedures for Computational Surface Thermochemistry," *Journal of Thermophysics and Heat Transfer*, Vol. 8, No. 1, 1994. https://doi.org/10.2514/3.497.

[24] Martin, A., Zhang, H., and Tagavi, K. A., "An introduction to the derivation of surface balance equations without the excruciating pain," *International Journal of Heat and Mass Transfer*, Vol. Technical Note, No. 115, 2017. https://doi.org/10.1016/j.ijheatmasstransfer.2017.07.078.

[25] Chen, Y.-K., Milos, F., and Gökçen, T., "Loosely Coupled Simulation for Two-Dimensional Ablation and Shape Change," *AIAA Journal*, Vol. 47, No. 5, 2010. https://doi.org/10.2514/1.39667.

[26] Bellas-Chatzigeorgis, G., "Development of advanced gas-surface interaction models for chemically reacting flows for re-entry conditions," Ph.D. thesis, Politecnico di Milano, 2018.

[27] Park, C., *Nonequilibrium Hypersonic Aerothermodynamics*, John Wiley and Sons, 1989.

[28] Ramshaw, J. D., "Self-Consistent Effective Binary Diffusion in Multicomponent Gas Mixtures," *Journal of Non-Equilibrium Thermodynamics*, Vol. 15, No. 3, 1990. https://doi.org/10.1515/jnet.1990.15.3.295.

[29] Giovangigli, V., *Multicomponent flow modeling*, Birkhäuser Basel, 1999. https://doi.org/10.1007/978-1-4612-1580-6.

[30] Cruden, B. A., Prabhu, D. K., Borner, A., Meurisse, J., Thornton, J., and Bellas-Chatzigeorgis, G., "Assessment of the Fluid Dynamics Boundary Condition in Ablating or Blowing Flows," *AIAA Paper 2023-2514*, 2023. https://doi.org/10.2514/6.2023-3614.

[31] Bianchi, D., "Modeling of ablation phenomena in space applications," Ph.D. thesis, La Sapienza, 2008.

[32] Kays, W., Crawford, M., and Weigand, B., *Convective Heat and Mass Transfer*, McGraw-Hill, 2005.

[33] Darcy, H., "Les fontaines publiques de la ville de Dijon," 1856.

[34] Scoggins, J. B., Leroy, V., Bellas-Chatzigeorgis, G., Dias, B., and Magin, T. E., "Mutation++: MUlticomponent Thermodynamics And Transport properties of IONized gases in C++," *SoftwareX*, Vol. 12, No. 100575, 2020.

[35] Bellas Chatzigeorgis, G., Haskins, J. B., and Scoggins, J. B., "Transport properties for neutral C, H, N, O, and Si-containing species and mixtures from the Gordon and McBride thermodynamic database," *Physics of Fluids*, Vol. 34, No. 8, 2022, p. 087106. https://doi.org/10.1063/5.0098060.

[36] Park, C., "Effects of atomic oxygen on graphite ablation," *AIAA Journal*, Vol. 11, No. 14, 2020. https://doi.org/10.2514/3.7267.

[37] Zhluktov, S. V., and Abe, T., "Viscous shock-layer simulation of airflow past ablating blunt body with carbon surface," *J. Thermophysics Heat Transfer*, Vol. 13, No. 1, 1999, pp. 50–59. https://doi.org/10.2514/2.6400.

[38] Poovathingal, S., Schwartzentruber, T. E., Murray, V. J., and Minton, T. K., "Molecular simulation of carbon ablation using beam experiments and resolved microstructure," *AIAA J.*, Vol. 54, No. 3, 2016, pp. 999–1010. https://doi.org/10.2514/1.J054562.

[39] Poovathingal, S., Schwartzentruber, T. E., Murray, V. J., Minton, T. K., and Candler, G. V., "Finite-rate oxidation model for carbon surfaces from molecular beam experiments," *AIAA J.*, Vol. 55, No. 5, 2017, pp. 1644–1658. https://doi.org/10.2514/1.J055371.

[40] Chen, Y. K., and Gökçen, T., "Evaluation of Finite-Rate Gas/Surface Interaction Models for Carbon-Based Ablator," *Journal of Spacecraft and Rockets*, Vol. 53, No. 1, 2016. https://doi.org/10.2514/1.A33377.

[41] Candler, G. V., "Nonequilibrium Processes in Hypervelocity Flows: An Analysis of Carbon Ablation Models," *AIAA Paper 2012-0724*, 2012. https://doi.org/10.2514/6.2012-724.

[42] Chen, Y. K., and Gökçen, T., "Effect of Nonequilibrium Surface Thermochemistry in Simulation of Carbon-Based Ablators," *Journal of Spacecraft and Rockets*, Vol. 50, No. 5, 2013. https://doi.org/10.2514/1.A32451.

[43] Candler, G., Alba, C. R., and Greendyke, R. B., "Characterization of Carbon Ablation Models Including Effects of Gas-Phase Chemical Kinetics," *Journal of Thermophysics and Heat Transfer*, Vol. 31, No. 3, 2017. https://doi.org/10.2514/1.T4752.

[44] Prata, K. S., Schwartzentruber, T. E., and Minton, T. K., "Air-Carbon Ablation Model for Hypersonic Flight from Molecular-Beam Data," *AIAA Journal*, Vol. 60, No. 2, 2022. https://doi.org/10.2514/1.J060516.

[45] Murray, V. J., Marshall, B. C., Woodburn, P. J., and Minton, T. K., "Inelastic and Reactive Scattering Dynamics of Hyperthermal O and O 2 on Hot Vitreous Carbon Surfaces," *Journal of Physical Chemistry*, Vol. 119, No. 26, 2015, pp. 14780–14796. https://doi.org/10.1021/acs.jpcc.5b00924.

[46] Murray, V. J., and Minton, T. K., "Gas-Surface Interactions of Atomic Nitrogen with Vitreous Carbon," *Carbon*, Vol. 150, 2019, pp. 85–92. https://doi.org/10.1016/j.carbon.2019.04.117.

[47] Keenan, J. A., and Candler, G. V., "Simulation of Graphite Sublimation and Oxidation under Re-Entry Conditions," *AIAA Paper 1994-2083*, 1994. https://doi.org/10.2514/6.1994-2083.

[48] Kuntz, D., Hassan, B., and Potter, D., "Evaluation of Sublimation Kinetics for Phenolic Impregnated Carbon Ablator," *Journal of Thermophysics and Heat Transfer*, Vol. 15, No. 2, 2001. https://doi.org/10.2514/2.6594.

[49] Chen, Y. K., and Gökçen, T., "Evaluation of Sublimation Kinetics for Phenolic Impregnated Carbon Ablator," *Journal of Spacecraft and Rockets*, Vol. 59, No. 5, 2022. https://doi.org/10.2514/1.A35424.

[50] Marschall, J., and MacLean, M., "Finite-Rate Surface Chemistry Model, I: Formulation and Reaction System Examples," *AIAA Paper 2011-3783*, 2011. https://doi.org/10.2514/6.2011-3783.

[51] Eriksson, L. E., "Generation of boundary-conforming grids around wing-body configurations using transfinite interpolation," *AIAA Journal*, Vol. 20, No. 10, 1982. https://doi.org/10.2514/3.7980.

[52] Batina, J. T., "Unsteady Euler algorithm with unstructured dynamic mesh for complex-aircraft aerodynamic analysis," *AIAA Journal*, Vol. 3, No. 29, 1991, pp. 327–333. https://doi.org/10.2514/3.10583.

[53] Droba, J., "Tangle-Free Finite Element Mesh Motion for Ablation Problems," *AIAA Paper 2016-3386*, 2016. https://doi.org/10.2514/6.2016-3386.

[54] Farhat, C., Degand, C., Koobus, B., and Lesoinne, M., "Torsional springs for two-dimensional dynamic unstructured fluid meshes," *Computational Methods in Applied Mechanics and Engineering*, Vol. 163, 1998. https://doi.org/10.1016/S0045-7825(98)00016-4.

[55] Loehner, R., and Yang, C., "Improved ALE mesh velocities for moving bodies," *Communications in Numerical Methods in Engineering*, Vol. 12, 1996, pp. 599–608. https://doi.org/10.1002/(SICI)1099-0887(199610).

[56] Helenbrook, B., "Mesh deformation using the biharmonic operator," *International Journal for Numerical Methods in Engineering*, Vol. 56, 2003, pp. 1007–1021. https://doi.org/10.1002/nme.595.

[57] Liu, X., Qin, N., and Xia, H., "Fast dynamic grid deformation based on delaunay graph mapping," *Journal of Computational Physics*, Vol. 211, 2006, pp. 405–423. https://doi.org/10.1016/j.jcp.2005.05.025.

[58] Beckert, A., and Wendland, H., "Multivariate interpolation for fluid–structure-interaction problems using radial basis functions," *Aerospace Science and Technology*, Vol. 5, 2001, pp. 125–134. https://doi.org/10.1016/S1270-9638(00)01087-7.

[59] Buhmann, M., *Radial Basis Functions*, Cambridge University Press, 2005.

[60] A. de Boer, H. B., M.S. dan der Shoot, "Mesh deformation based on radial basis function interpolation," *Computers and Structures*, Vol. 85, 2007, pp. 784–795. https://doi.org/10.1016/j.compstruc.2007.01.013.

[61] Driver, D. M., Olson, M. E., Barnhardt, M. D., and MacLean, M., "Understanding High Recession Rates of Carbon Ablators Seen in Shear Tests in an Arc Jet," *AIAA Paper 2010-1177*, 2010. https://doi.org/10.2514/6.2010-1177.

[62] Driver, D. M., Carballo, J. E., Beck, R., Prabhu, D., Santos, J. A., Cassel, A., Skokova, K., Tang, C., Hwang, H. H., Slimko, E., Wilcockson, W., and Songer, J., "Arc Jet Testing in a Shear Environment for Mars Science Laboratory Thermal Protection System," *Journal of Spacecraft and Rockets*, 2014. https://doi.org/10.2514/1.A32728.